REPORT DOCUMENTATION PAGE

Public reporting burden for this collection of information is estimated to average 1 hour per response, including the time for reviewing instructions, data needed, and completing and reviewing this collection of information. Send comments regarding this burden estimate or any other aspect of this collection of information, including suggestions for reducing this burden to Department of Defense, Washington Headquarters Services, Directorate for Information Operations and Reports (0704-0188), 1215 Jefferson Davis Highway, Suite 1204, Arlington, VA 22202-4302. Respondents should be aware that notwithstanding any other provision of law, no person shall be subject to any penalty for failing to comply with a collection of information if it does not display a currently valid OMB control number. **PLEASE DO NOT RETURN YOUR FORM TO THE ABOVE ADDRESS.**

1. REPORT DATE (DD-MM-YYYY) 16-02-2009	2. REPORT TYPE FINAL	3. DATES COVERED (From - To) 1-12-2007 – 30-11-2008

4. TITLE AND SUBTITLE
"Tightly-Integrated LADAR/INS Algorithm Development to Support Urban Operations"

5a. CONTRACT NUMBER

5b. GRANT NUMBER
FA9550-07-1-0383

5c. PROGRAM ELEMENT NUMBER

6. AUTHOR(S)
Dr. Maarten Uijt de Haag, Dr. Zhen Zhu, Dr. Andrey Soloviev, Dr. Frank van Graas

5d. PROJECT NUMBER

5e. TASK NUMBER
07NE174

5f. WORK UNIT NUMBER

7. PERFORMING ORGANIZATION NAME(S) AND ADDRESS(ES)
Ohio University
105 Research & Technology
Center
Athens, OH 45701

8. PERFORMING ORGANIZATION REPORT NUMBER

9. SPONSORING / MONITORING AGENCY NAME(S) AND ADDRESS(ES)
AF Office of Scientific
Research
875 N. Randolph St. Room 3112
Arlington, VA 22203

10. SPONSOR/MONITOR'S ACRONYM(S)

11. SPONSOR/MONITOR'S REPORT NUMBER(S)

12. DISTRIBUTION / AVAILABILITY STATEMENT

Public

13. SUPPLEMENTARY NOTES

14. ABSTRACT
There is a need to provide our forces with a much-needed navigation capability for operations in urban environments where GPS is not available due to shielding, excessive errors due to multipath and the proliferation of new GPS jamming techniques. Accurate and precise pervasive positioning is one of the key enablers for urban warfare. This capability is crucial in placing the right sensor on the right target at the right time in a multi-sensor/platform system. This capability is also needed for sensor cross-cueing, which is essential to integrated operation and optimal use of resources and will be a game changer for urban operations.

The proposed method consists of a tightly integrated Laser radar (LADAR) and Inertial sensor to achieve positioning at the sub-meter level in addition to attitude determination and obstacle avoidance. The tight integration enables high performance feature extraction and association, not possible with prior LADAR systems. The proposed system can work with partial map and no map information.

In year 2 of this effort we extended the 2D LADAR/INS mechanization for urban position and heading determination of year 1 to three dimensions (3D), further developed the algorithms for integrity calculation using LADAR/INS integration, and setup the data collection system on a four-rotor UAV for algorithm validation purposes.

15. SUBJECT TERMS
Tightly-Integrated Ladar; Navigation capability for operations in urban environments;

16. SECURITY CLASSIFICATION OF:			17. LIMITATION OF ABSTRACT	18. NUMBER OF PAGES	19a. NAME OF RESPONSIBLE PERSON Zofia Starzyk
a. REPORT U	b. ABSTRACT U	c. THIS PAGE U	UL	49	19b. TELEPHONE NUMBER (include area code) (740) 593-1512

Standard Form 298 (Rev. 8-98)
Prescribed by ANSI Std. Z39.18

Tightly-Integrated LADAR/INS Algorithm Development to Support Urban Operations

FINAL REPORT

YEAR 2

by

Maarten Uijt de Haag
Zhen Zhu
Andrey Soloviev .
Frank van Graas

Ohio University
Avionics Engineering Center, Russ College of Engineering and Technology
School of Electrical Engineering and Computer Science
Avionics Engineering Center
Athens, OH 45701

Submitted to

20090410040

Table of Contents

Abstract

There is a need to provide our forces with a much-needed navigation capability for operations in urban environments where the Global Positioning System (GPS) is not available due to shielding, excessive errors due to multipath and the proliferation of new GPS jamming techniques. Accurate and precise pervasive positioning is one of the key enablers for urban warfare. This capability is crucial in placing the right sensor on the right target at the right time in a multi-sensor/platform system. This capability is also needed for sensor cross-cueing, which is essential to integrated operation and optimal use of resources and will be a game changer for urban operations.

The proposed method consists of a tightly integrated Laser radar (LADAR) and Inertial sensor to achieve positioning at the sub-meter level in addition to attitude determination and obstacle avoidance. The tight integration enables high performance feature extraction and association, not possible with prior Ladar systems. Furthermore, the proposed system can work with partial map and no map information.

Today, LADAR sensors are used for indoor and outdoor mapping, obstacle avoidance, and are being considered for surveillance under foliage. However, use of LADAR for navigation applications has only recently become feasible since LADAR technology has matured in the past few years to an acceptable level, i.e. hundred-meter range, mm resolution, low-cost, eye-safe; Field Programmable Gate Array (FPGA) technology can now handle the data processing and interfacing loads.

In year 2 of this effort we extended the 2D LADAR/INS mechanization for urban position and heading determination of year 1 to three dimensions (3D), further developed the algorithms for integrity calculation using LADAR/INS integration, and setup the data collection system on a four-rotor UAV for algorithm validation purposes.

Milestones (M) /Deliverables (D)	M	D
Task 2.1 *Development of algorithms for real-time urban 3D position and attitude estimation using LADAR/INS integration.*	X	
Task 2.2: *Data collection with the 4-rotor UAV in an urban environment.*	X	
Final Report on Phase 2		X

1.   Introduction

There is a need to provide our forces with a much-needed navigation capability for operations in urban environments where GPS is not available due to shielding, excessive errors due to multipath and the proliferation of new GPS jamming techniques. Accurate and precise pervasive positioning is one of the key enablers for urban warfare. An illustration of navigation in an urban environment is shown in Figure 1.
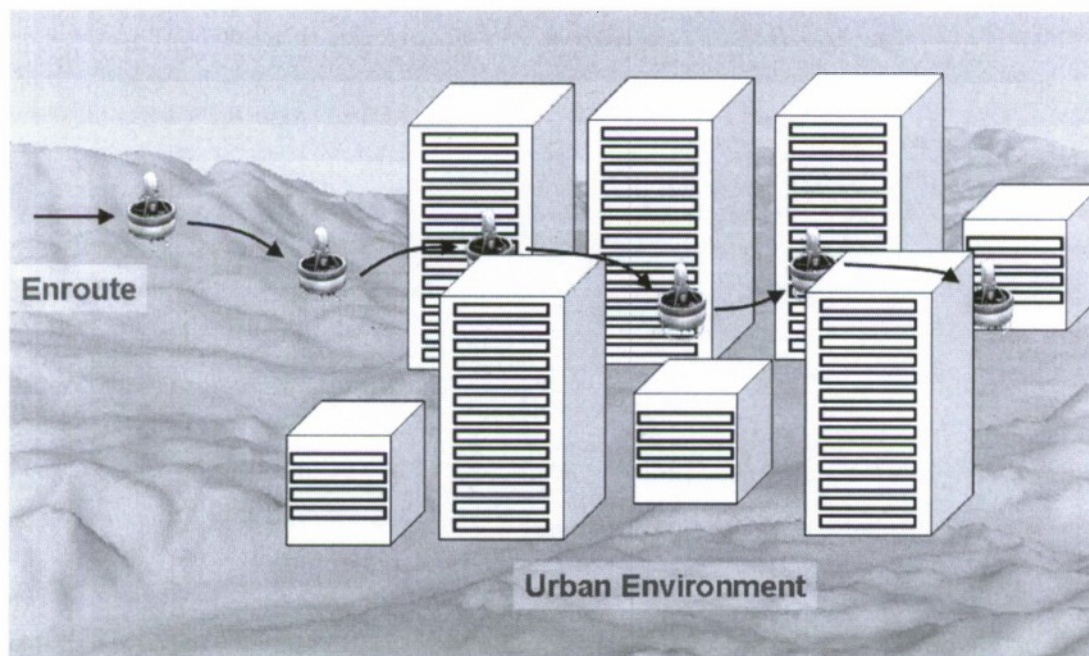

Figure 1. Navigation of a UAV in an urban environment.

To accomplish the positioning task, urban navigators currently use primarily GPS with map-aiding and/or odometry and gyros, beacon/Wi-Fi based localization systems, assisted GPS with HDTV or base stations, or Digital Scene Matching Area Correlation (DSMAC). Existing terrain navigators are not applicable for the urban environment. None of the existing systems achieve sub-meter positioning accuracies in challenging urban environments.

The main challenges for Radio Frequency (RF) based systems such as GPS or radio-beacon based systems are denial (intentional, unintentional, and shielding/shadowing) and severe multipath. Furthermore, these systems require an external infrastructure and detailed maps of the urban environment.

The proposed solution to the urban navigation problem is the tight integration of LADAR and inertial, i.e. Inertial is used to stabilize the LADAR at the cm-level, the LADAR map is then used to calibrate the Inertial at the cm-level. The resulting system has sub-meter level relative positioning performance. The focus of the proposed algorithm development will be

on the mathematical rigor associated with the positioning and integrity algorithms.

The proposed LADAR/INS research is divided into the following research thrusts:

- Tight LADAR/INS integration mechanization
- 2-D line navigation
- 3-D line navigation
- Real-time feature extraction/association/mapping
- Processing requirements

This final report will address the year 2 developments of this effort; the development of algorithms for real-time urban 3D position and attitude estimation using LADAR/INS integration (task 2.1); preparation for a data collection with the 4-rotor UAV in an urban environment (task 2.2); also the algorithms for integrity calculation using LADAR/INS integration were further developed. The following articles related to the work performed under this research effort were accepted for publication:

A. Soloviev, M. Uijt de Haag, "An Autonomous Integrity Monitor for Detection and Isolation of Moving Features in Laser Scanner-based Navigation," *IEEE Transactions of Aerospace and Electronic Systems*, Provisionally accepted for publication with minor revisions[1], 2008.

M. Stepaniak, F. van Graas, M. Uijt de Haag, "Design Considerations for a Large Payload Quadrotor," *AIAA Journal of Aircraft*, Accepted for publication, 2008.

A. Soloviev, M. Uijt de Haag, "Three-Dimensional Navigation of Autonomous Vehicles Using Scanning Laser Radars: Concept and Initial Verification," *IEEE Transactions of Aerospace and Electronic Systems*, Accepted for publication, 2008.

M. Stepaniak, M. Uijt de Haag, F. van Graas, "Field Programmable Gate Array-Based Attitude Stabilization," *AIAA Journal of Aerospace Computing, Information, and Communication,* Provisionally accepted for publication with minor revisions, 2008.

Note that this list includes work performed by Maj. Michael Stepaniak, Ph.D, which he performed in support of this research as an Ohio University Ph.D. student from the Air Force resulting in the following dissertation:

Michael J. Stepaniak, "A Quadrotor Sensor Platform," Ph.D. Dissertation, Ohio University, August 2008.

Currently, Dr. Stepaniak is with the faculty of the Air Force Institute of Technology School of Engineering.

2. Background

The majority of previous research related to the use of laser scanners for autonomous navigation in indoor and urban outdoor environments has been for robotic localization with most approaches attempting to improve solutions to the so-called Simultaneous Localization and Mapping (SLAM) problem. SLAM using 2D laser scans has been

performed utilizing a number of different methods such as using extracted corners formed by the intersection of two walls [2], extracted lines [3][4][5], and in conjunction to retro-reflective beacons in known or unknown locations [6]. Although some work has been conducted to address necessary topics such as the estimation and use of error covariance [4][5][7][8], most methods of navigation using laser scanners are ad hoc, with minimal analysis of the confidence, accuracy, integrity, or integration of the solution with other sensors. In [9], the authors report loose coupling of the INS and two airborne laser scanners for terrain-based navigation in unknown environments.

While most existing approaches are only loosely coupled with odometery, an integration of 2D laser scans with GPS in the range-domain (generally referred to as tight coupling) is reported in [10]. Tight coupling of GPS, INS and an electro optical (EO) sensor is reported in [11].

This report applies integrity monitoring techniques for assured detection and isolation of moving features. These techniques exploit redundancy in feature geometry for solving the detection/isolation problem. Essentially, incorporation of moving features into the navigation solution is considered as a faulty measurement case. Redundant features are applied to monitor integrity of the laser-based navigation solution and to detect and isolate faulty measurements created by moving features. Detection and isolation of faulty measurements using measurement redundancy is widely utilized in the area of GPS for autonomous integrity monitoring of GPS receivers [12][13][14][15]. This report adopts GPS integrity monitoring techniques to the area of LADAR-based navigation in order to detect and isolate moving features. Application of an integrity monitoring approach allows for 1) efficient detection and isolation of even very slowly moving features (sub-cm/s feature velocities); and, 2) assignment of confidence levels to the detection and isolation process: i.e., a probability that a feature velocity that exceeds the detection protection level will be undetected does not exceed a specified threshold (e.g., 10^{-5}).

3. Development of algorithms for real-time urban 3D position and attitude estimation using LADAR/INS integration. (Year 2 Task 2.1)

3.1 Introduction and basic concepts

While year 1 focused on performing 2D navigation with integrated LADAR and INS, year 2 focused on extending these concepts to three dimensions using only 2D LADAR scans. Again, lines were chosen as the basic feature representation, but this time consecutive lines were used to form planar surfaces that were then used to perform 3D navigation. The rationale for the use of planar surfaces for navigation in 3D urban environments is that planes are common in man-made environments. To exemplify, Figure 2 shows typical urban indoor (hallway) and outdoor (urban canyon) images. Multiple planes can be extracted from both images as illustrated in Figure 2. Since changes in image feature parameters between two different scans are used for navigation, this feature must be observed in both scans. Feature repeatability is thus essential for the LADAR-based navigation. Planar surfaces satisfy this requirement, as they are highly repeatable from scan

6

to scan. If a wall of a building stays in the LADAR measurement range and FoV then the plane associated with that wall repeats in the scan images.
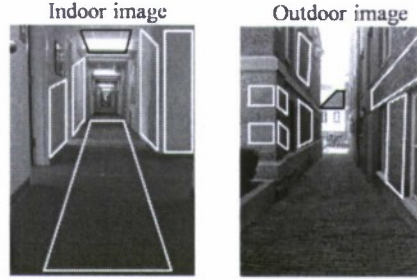

Figure 2. Examples of planar surfaces observed in urban images: multiple planes can be extracted for indoor and outdoor image examples

Given that the sensor system observes N planar surfaces P_i (in the camera frame) from the 3D image and that each planar surface is characterized by its centroid $\mathbf{p}_{0,i}$ and normal vector $\mathbf{n}_i$. From these two parameters, one can find the closest distance (or plane range) from the camera origin to the planar surface P_i according to:

$$\rho_i = \left| \mathbf{p}_{0,i} \cdot \mathbf{n}_i \right| \tag{1}$$

Note that from equation (1) one could also derive an expression for the normal point on planar surface P_i :

$$\mathbf{p}_{n,i} = \mathbf{x} - \text{sign}(\mathbf{p}_{0,i} \cdot \mathbf{n}_i)\mathbf{n}_i \tag{2}$$

Given the closest distance from the camera origin to the planar surface and the normal vector expressed in the camera frame at time epochs t_k and t_{k+1}, the change in distance to the planar surface can be related to the normal vector and the change in user position according to:

$$\begin{aligned} \Delta\rho_i &= \rho_i[t_{k+1}] - \rho_i[t_k] \\ &= \Delta\mathbf{x} \cdot \mathbf{n}_i \end{aligned} \tag{3}$$

This relationship is illustrated in the geometry depiction in Figure 3. Given N planar surfaces, the N equations for the planar surfaces can be rewritten in the following matrix form:

$$\begin{bmatrix} \mathbf{n}_1^T \\ \vdots \\ \mathbf{n}_N^T \end{bmatrix} \Delta\mathbf{x} = \begin{bmatrix} \Delta\rho_1 \\ \vdots \\ \Delta\rho_N \end{bmatrix} \Rightarrow \mathbf{A}\Delta\mathbf{x} = \Delta\rho \tag{4}$$
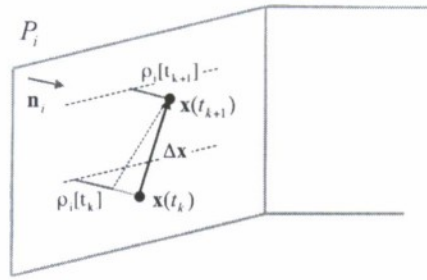
7

Figure 3. Relation between position change and distance

A solution to equation (4) does exist only if matrix **A** has 3 or more independent rows. Given that each row consists of a normal vector, this means that the observing sensor must observe at least three non-parallel surfaces in the environment. In that case the solution to equation (4) can be obtained using any least squares implementation such as the normal equations, the QR decomposition, the singular value decomposition (SVD), or total least squares. Using the QR decomposition, the estimate for the position change is given by:

$$\Delta \hat{\mathbf{x}} = \mathbf{R}_U^{-1} \mathbf{Q}_U^T \Delta \rho \tag{5}$$

where **A** = **QR** with residual errors:

$$\mathbf{e} = \mathbf{Q}_L^T \Delta \rho \tag{6}$$

The scenario in which parallel planar surfaces do exist and not enough normal vectors are available for position change computation can be detected by inspection of the diagonal elements and rank of the **R** matrix. An example of such a situation would be the observation of the hallway depicted in Figure 2; if the end of the hallway can somehow not be observed only observability in two dimensions could be achieved. Integration with an IMU would be required to maintain a position solution during these outages. Note that the partial geometry information could still be used for integration with the IMU.

The estimation of the change in attitude of the camera from one frame to the next can be derived from the change in orientation of the normal vectors as expressed in the camera coordinate frame since the environment is assumed to be stationary. The normal vector at time epoch t_{k+1} can be related to the normal vector at time epoch t_k via a Direction Cosine Matrix (DCM) as depicted in Figure 4.

$$\mathbf{n}_i(t_{k+1}) = \mathbf{C}_{b(t_k)}^{b(t_{k+1})} \mathbf{n}_i(t_k) \tag{7}$$

This DCM, $\mathbf{C}_{b(t_k)}^{b(t_{k+1})}$ is directly related to the attitude change of the camera in the navigation frame. The problem of estimating the attitude change of the camera platform is now equivalent to the problem of finding the matrix $\mathbf{C}_{b(t_k)}^{b(t_{k+1})}$ that maximizes the dot product of the left and right hand sides of equation (7), or

$$C_{b(t_k)}^{b(t_{k+1})}\mathbf{n}_i(t_k) \cdot \mathbf{n}_i(t_{k+1}) \tag{8}$$

For N normal vectors corresponding to N planar surfaces, all N dot products (8) can be added resulting in the following metric:

$$F = \sum_{i=1}^{N} C_{b(t_k)}^{b(t_{k+1})}\mathbf{n}_i(t_k) \cdot \mathbf{n}_i(t_{k+1}) \tag{9}$$

The DCM estimate is thus given by:

$$\hat{C}_{b(t_k)}^{b(t_{k+1})} = \arg \max_{C_{b(t_k)}^{b(t_{k+1})}} \left\{ \sum_{i=1}^{N} C_{b(t_k)}^{b(t_{k+1})}\mathbf{n}_i(t_k)\mathbf{n}_i(t_{k+1}) \right\} \tag{10}$$

from which changes in pitch, roll and yaw can be found directly. To estimate the rotation matrix, a minimum of two non-parallel planar surfaces is required. It can be shown that equation (10) results in the least squares estimate of $C_{b(t_k)}^{b(t_{k+1})}$.

A direct solution to equation (10) is discussed in [16], whereas [17] uses quaternions instead of the DCMs to calculate the three Euler angles. More about finding the attitude change in section 3.5.

Note that a correct correspondence of planar surfaces is a necessity for the method to result in a reliable estimate of change in attitude.
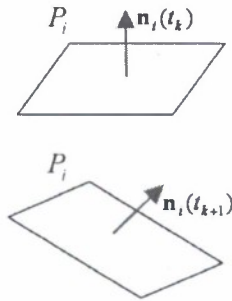

Figure 4. Change in normal vector orientation

Figure 5 illustrates a generic navigation routine that exploits planar surfaces to derive the navigation solution. A 3D scan image of the environment is obtained by a scanning LADAR. Planes are extracted from LADAR images and used to estimate the navigation solution that is comprised of changes in LADAR position and orientation between scans. In order to use a planar surface for the estimation of position and orientation changes from one scan to the next, this planar surface must be observed in both scans and it must be known with certainty that the plane in one scan corresponds to the plane in the next scan.

Hence, the feature matching procedure establishes a correspondence between planes extracted from the current scan and planes extracted from previous scans. The navigation routine stores planes extracted from previous scans into the plane list. The plane list is initially populated at the initial scan. If a new plane is observed during one of the following scans, the plane list is updated to include this new plane.

Figure 5. Generic routine of 3D navigation that uses images of a scanning LADAR

In the final report of last year as well as reference [18], INS data are exploited to match lines extracted from 2D LADAR images for a 2D navigation case. In order to use INS data for plane matching, line-matching algorithms developed in [18] must be extended for a 3D case. Hence, the feature matching procedure has to use position and orientation outputs of the INS to predict plane location and orientation in the current scan based on plane parameters observed in previous scans. If predicted plane parameters match closely to the parameters of the plane extracted from the current scan, a match is declared and a matched plane is used for navigation computations. Note that INS data can also be applied to compensate for LADAR motion during scans for those cases where such motion can introduce significant distortions to LADAR scan images. Following feature matching, changes in parameters of the planes that are matched between different scans are exploited to estimate the navigation and attitude solution. Changes in plane parameters are also applied to periodically re-calibrate the INS to reduce drift terms in inertial navigation outputs in order to improve the quality of the INS-based plane prediction used by the feature matching procedure.

This year's effort focused on the key aspects of the planar based navigation that are related to LADAR data processing only. Development of LADAR/INS integrated components is currently underway. To obtain 3D planar surfaces from the environment 3D imaging sensor could be used, but these sensors are costly and currently not readily available. The following section will address the 3D imaging technology shortly. Since 2D LADAR scanners are readily available, two methods were investigated to use 2D LADAR scans to estimate planar surfaces. At the current time, both methods have not yet been compared,

but they are expected to be equivalent in performance, although the second method is easier to visualize. LADAR imaging technologies are discussed first.

3.2   Optical Sensors

Various optical approaches exist to obtain 3D imagery of the environment such as stereovision camera systems, the combination of a digital camera and projected light from a laser source, flash LADAR systems, and systems based on a LADAR scanning in both azimuth and elevation directions.

Flash LADAR sensors consist of a modulated laser emitter coupled with a focal plane array detector and the required optics. Similar to a conventional camera this sensor creates an "image" of the environment, but instead of producing a 2D image where each pixel has associated intensity values, the Flash LADAR generates an image where each pixel measurement consists of an associated range and intensity value. Current Flash LADAR technology is capable of greater than 100 x 100 pixel resolution with 5 mm depth resolution at a 30 Hz frame rate. And low-cost 3D imager solutions with less range accuracy (cm rather than mm) and range are available from commercial companies such as MESA Imaging, Canesta, Inc., and PMD Technologies GmbH. Even with a limited range of between 7 and 30m), these camera have application in our target indoor environment since the distances to the observed planar surfaces is limited as well. These cameras derive the range by measuring the phase difference (shift) between the transmitted and received (from the target) signal from a modulated light source and have a range limitation determined by the wavelength of the modulation. Other commercial sensors such as the sensors by Advanced Scientific Concepts, Inc. (ASC) measure the time-of-flight of a light pulse to compute distance. The advantage of all these 3D imaging sensors is the instantaneous acquisition of all pixels within the FoV. The disadvantage is their often-limited range and limited FoV. The limited FoV can significantly limit the availability of features that can be used for navigation. Note that the limited FoV mainly depends on the optics used for the camera and that a larger FoV results in a higher power requirement since the light source must provide the same light density over a larger spherical area.

3D imaging sensors based on scanning LADARs are also commercially available, for example, from Velodyne, AutonoSys, Riegl and Optech. In contrast to the flash LADAR sensors, these scanning systems require a large amount of optics and precise scanning mechanisms and are, therefore, often expensive. Since these systems are pulsed and have a very narrow instantaneous FoV, their ranges are longer and the range accuracy is higher. The FoV of these sensors is, furthermore, determined by the scanning mechanism and is in general much larger (as large as 360 deg). This type of scanners is designed primarily for mapping applications. The scan rate is generally slow (from few seconds to few minutes per FoV) due to extensive scans at different elevation angles, which is not required for navigation applications as shown in the following sections.

This report proposes a low-cost alternative to existing 3D scanning LADARs in order to develop and verify 3D navigation methods. An inexpensive 2D scanning LADAR (SICK

11

LMS-200) is augmented by a low-cost servomotor that enables LADAR rotations in a limited elevation range. The elevation range is chosen to allow for plane reconstruction as described in the next section. The 3D navigation methods described in this paper are also developed to meet the UAV payload requirements, since the limited elevation scan range allows for a simple and light sensor design and requires limited processing power of the LADAR data.

2D LADAR sensor imagery has been previously considered for 3D plane reconstruction in mapping applications. Particularly, in [19], 2D LADAR images are used to construct planar maps of indoor office environments. Specifically, [19] employs an upward looking 2D LADAR that is mounted on a robotic vehicle. Planar surfaces are extracted from multiple LADAR images that are collected as the robot moves through the indoor hallway. While [19] performs a 3D mapping, the navigation task is still carried out in two dimensions using data of a 2D forward-looking LADAR. As mentioned previously, the focus of this paper is 3D autonomous navigation as opposed to 3D mapping. Hence, the plane extraction method described in the following section is not optimized for mapping purposes but for estimation of the UAV 3D navigation solution from the changes in plane parameters between scans.

3.3 Plane Reconstruction using 2D LADAR Rotations in a Limited Elevation Range

The method for 3D navigation using 2D LADAR scans is based on deriving the parameters that define a planar surface from two or more LADAR scans. These scans can be obtained by simultaneously measuring multiple scans from LADAR sensors installed under different orientations on the UAV platform or by rotating a single LADAR scanner. We assume the latter configuration for the remainder of this report. LADAR first performs a scan at zero-rotation as shown in Figure 6.

Planar surface
(e.g. a building wall)
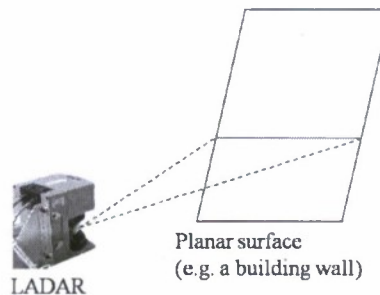
LADAR

Figure 6. Zero elevation scan: lines observed in the scan image are created by the intersection of the LADAR scanning beam with planar surfaces such as building walls

The LADAR scanning beam intersects with a planar surface created, for example, by a wall of a building. A line is obtained in the scan image as a result of this intersection. This line can be extracted from the scan image using line extraction techniques such as the ones reported in [20]. One line is obviously insufficient for the plane reconstruction since this line can belong to multiple planes as illustrated in Figure 7.
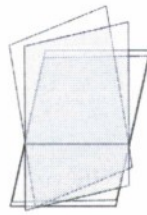
Figure 7. Zero elevation scan: multiple planes can be fit through a single line that is extracted from zero elevation scan; hence, one scan is insufficient for the plane reconstruction

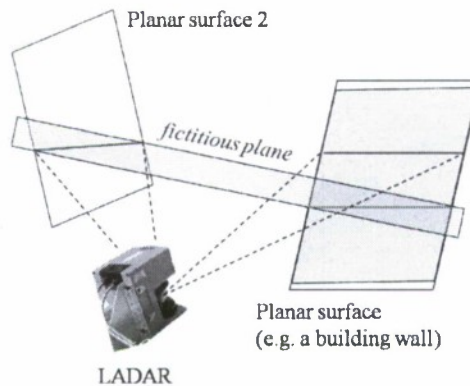The LADAR is thus rotated and a second scan is taken as shown in Figure 8.

Figure 8. First elevated scan: second intersect line is obtained for each planar surface in the LADAR FoV; fictitious planes can still exist since a plane can be fit through two lines that belong to different real planes

Two intersect lines are obtained after the rotated scan is performed: 1) intersection of the planar surface with the non-rotated LADAR scanning plane (Figure 6) and 2) intersection of the planar surface with the rotated LADAR scanning plane (Figure 8). These two lines are applied for the plane reconstruction. A plane reconstruction that is solely based on two lines can still be ambiguous. Particularly, if there is a second planar surface present within the FoV of the LADAR, a fictitious plane can be fit through two lines that belong to different real planes as illustrated in Figure 9. Hence, information contained in two LADAR images is insufficient to separate real and fictitious planes.

A third scan (second elevated scan) is taken to resolve the plane reconstruction ambiguity. Figure 9 illustrates the second elevated scan. A third intersect line is extracted from the third scan image. This line belongs to the real plane but does not belong to the fictitious plane. The fictitious plane is thus removed, which completes the plane reconstruction.
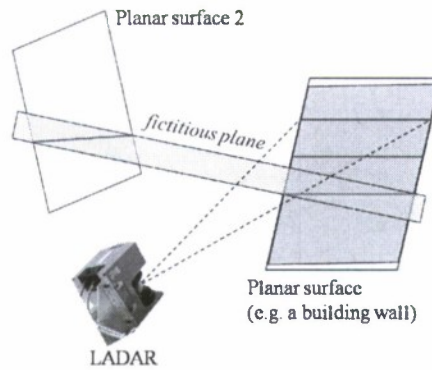
Figure 9. Second rotated scan: a third intersect line is extracted from the LADAR scan image; the use of this line allows for the removal of fictitious planes

The above consideration demonstrates that three consecutive LADAR scans (zero-rotation scan and two rotated scans) are sufficient for the reconstruction of planar surfaces. A formal description of the reconstruction procedure is offered next. Figure 10 illustrates the LADAR body frame.
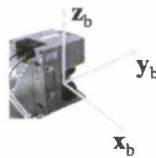

Figure 10. LADAR body frame: x_b and y_b axes lie in the scanning plane (x_b axis is in the direction of the zero scanning angle, y_b axis is in the direction of the 90-deg scanning angle), z_b axis is perpendicular to the scanning plane

Figure 11 represents a planar surface:
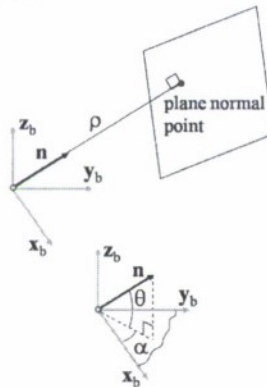
Figure 11. Representation of a planar surface

In Figure 11, **n** is the plane normal vector, which is the unit vector that originates from the LADAR body frame origin perpendicular to the planar surface; ρ is the plane range (as given in equation (1), which is the closest distance from the body-frame origin to the plane; θ is the plane tilt angle, which is the angle between the plane normal vector and the x_b, y_b

14

plane; α is the plane azimuth angle, which is the angle between the projection of **n** on the x_b, y_b plane and the x_b axis. Note that the plane normal vector is related to the plane angular parameters (azimuth and tilt angles) as follows:

$$\mathbf{n} = \begin{bmatrix} \cos(\alpha) \cdot \cos(\theta) \\ \sin(\alpha) \cdot \cos(\theta) \\ \sin(\theta) \end{bmatrix} \tag{11}$$

A plane can be also represented by its normal point where the normal point is the intersection of the plane and a line originating from the LADAR location perpendicular to the plane of interest.

Equation (12) formulates the plane equation in Cartesian coordinates:

$$\mathbf{p}_b \cdot \mathbf{n} = \rho \Rightarrow$$
$$x_b \cdot \cos(\alpha) \cdot \cos(\theta) + y_b \cdot \sin(\alpha) \cdot \cos(\theta) + z_b \cdot \sin(\theta) = \rho \tag{12}$$

where x_b, y_b, and z_b are the Cartesian coordinates of any point, $\mathbf{p}_b$, that belongs to the plane, these coordinates are expressed in the LADAR body frame.

Figure 12 shows lines of intersection of LADAR scanning plane with the planar surface being reconstructed for cases of zero elevation scan and elevated scan.
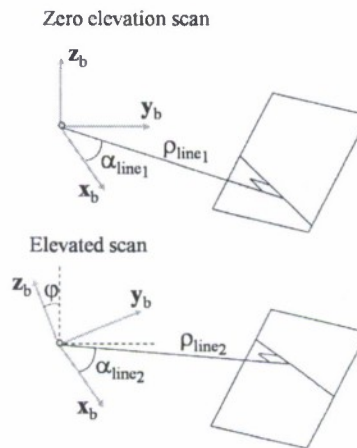
Figure 12. Intersections of the planar surface with non-elevated and elevated LADAR scanning planes; for the elevated scan, the LADAR is rotated about its x_b axis on angle φ

Using a polar line representation, the intersect line for the zero elevation scan is expressed as follows:

$$x_b \cdot \cos(\hat{\alpha}_{line_1}) + y_b \cdot \sin(\hat{\alpha}_{line_1}) = \hat{\rho}_{line_1} \tag{13}$$

In (13), $\hat{\alpha}_{line_1}$ is the line angle and $\hat{\rho}_{line_1}$ is the line range. Note that $\hat{\alpha}_{line_1}$ and $\hat{\rho}_{line_1}$ are estimated by a line extraction procedure (e.g., by an iterative split and merge procedure [20]) that is applied to LADAR scan data for the zero elevation scan. The intersect line should also satisfy the equation of intersection of the planar surface with the LADAR scanning plane (a horizontal plane $z_b = 0$, in this case). A corresponding equation of the intersect line is given below:

$$x_b \cdot \cos(\alpha) \cdot \cos(\theta) + y_b \cdot \sin(\alpha) \cdot \cos(\theta) + z_b \cdot \sin(\theta) = \rho$$
$$z_b = 0 \tag{14}$$

or:

$$x_b \cdot \cos(\alpha) \cdot \cos(\theta) + y_b \cdot \sin(\alpha) \cdot \cos(\theta) = \rho \tag{15}$$

Dividing both sides of equation (15) by $\cos(\theta)$ yields:

$$x_b \cdot \cos(\alpha) \cdot + y_b \cdot \sin(\alpha) = \frac{\rho}{\cos(\theta)} \tag{16}$$

Comparison of equations (13) and (16) allows relating estimates of the intersect line parameters with parameters of the planar surface:

$$\hat{\alpha} = \hat{\alpha}_{line_1}$$
$$\frac{\hat{\rho}}{\cos(\hat{\theta})} = \hat{\rho}_{line_1} \tag{17}$$

Equation (17) partially formulates the planar surface based on zero elevation scan data. A tilted scan is employed next to complete the plane formulation. The LADAR is rotated around its x_b axis on the φ angle for the tilted scan case. Equation (18) defines the equation of the coordinate transformation from the elevated LADAR frame (x'_b, y'_b, z'_b) into the zero elevation frame:

$$x_b = x'_b$$
$$y_b = \cos(\varphi) \cdot y'_b - \sin(\varphi) \cdot z'_b \tag{18}$$
$$z_b = \sin(\varphi) \cdot y'_b + \cos(\varphi) \cdot z'_b$$

Substitution of the coordinate transformation equation (18) into the plane equation (12) provides the plane equation expressed at the elevated LADAR frame:

$$x'_b \cdot \cos(\alpha) \cdot \cos(\theta) + y'_b \cdot \left(\sin(\alpha) \cdot \cos(\theta) \cdot \cos(\varphi) + \sin(\theta) \cdot \sin(\varphi) \right)$$
$$+ z'_b \cdot \left(\sin(\theta) \cdot \cos(\varphi) - \sin(\alpha) \cdot \cos(\theta) \cdot \sin(\varphi) \right) = \rho \tag{19}$$

This plane intersects with the LADAR scanning plane at $z'_b = 0$. The intersect line equation is thus expressed as follows:

16

$$x'_b \cdot \cos(\alpha) \cdot \cos(\theta) + y'_b \cdot \left(\sin(\alpha) \cdot \cos(\theta) \cdot \cos(\varphi) + \sin(\theta) \cdot \sin(\varphi)\right) = \rho \qquad (20)$$

This line can be also expressed using line parameters estimated from the elevated scan image. The expression is similar to equation (19) above:

$$x'_b \cdot \cos(\alpha_{line_2}) + y'_b \cdot \sin(\alpha_{line_2}) = \rho_{line_2} \qquad (21)$$

Equations (20) and (21) formulate the intersect line equation using plane parameters and parameters of the line (range and angle) determined from LADAR data, correspondingly. Evaluating equations (20) and (21) at $x'_b = 0$ yields:

$$x'_b = 0 \Rightarrow y'_b = \frac{\rho}{\left(\sin(\alpha) \cdot \cos(\theta) \cdot \cos(\varphi) + \sin(\theta) \cdot \sin(\varphi)\right)}$$
$$x'_b = 0 \Rightarrow y'_b = \frac{\hat{\rho}_{line_2}}{\cos(\hat{\alpha}_{line_2})} \qquad (22)$$

From equation (22) it follows:

$$\frac{\rho}{\left(\sin(\alpha) \cdot \cos(\theta) \cdot \cos(\varphi) + \sin(\theta) \cdot \sin(\varphi)\right)} = \frac{\hat{\rho}_{line_2}}{\cos(\hat{\alpha}_{line_2})} \qquad (23)$$

Substitution of equation (7) into (13) provides the following expression:

$$\frac{\hat{\rho}_{line_1} \cdot \cos(\theta)}{\left(\sin(\hat{\alpha}_{line_1}) \cdot \cos(\theta) \cdot \cos(\varphi) + \sin(\theta) \cdot \sin(\varphi)\right)} = \frac{\hat{\rho}_{line_2}}{\cos(\hat{\alpha}_{line_2})} \qquad (24)$$

or:

$$\frac{\hat{\rho}_{line_1}}{\left(\sin(\hat{\alpha}_{line_1}) \cdot \cos(\varphi) + tg(\theta) \cdot \sin(\varphi)\right)} = \frac{\hat{\rho}_{line_2}}{\cos(\hat{\alpha}_{line_2})} \qquad (25)$$

The plane tilt angle is thus related to the estimates of intersect line parameters obtained from the zero elevation scan and the elevated scan:

$$tg(\theta) = \frac{\hat{\rho}_{line_1} \cdot \cos(\hat{\alpha}_{line_2}) - \hat{\rho}_{line_2} \cdot \sin(\hat{\alpha}_{line_1}) \cdot \cos(\varphi)}{\hat{\rho}_{line_2} \cdot \sin(\varphi)} \qquad (26)$$

A combined use of equations (17) and (26) completes the formulation of the planar surface:

$$\hat{\alpha} = \hat{\alpha}_{line_1}$$

$$\hat{\theta} = \text{arctg}\left(\frac{\hat{\rho}_{line_1} \cdot \cos(\hat{\alpha}_{line_2}) - \hat{\rho}_{line_2} \cdot \sin(\hat{\alpha}_{line_1}) \cdot \cos(\varphi)}{\hat{\rho}_{line_2} \cdot \sin(\varphi)} \right) \qquad (27)$$

$$\hat{\rho} = \hat{\rho}_{line_1} \cdot \cos(\hat{\theta})$$

As mentioned previously, a second rotated scan is applied to remove fictitious planes. Fictitious planes can be created by fitting a plane through two lines that belong to different real planes. To remove fictitious planes, equation (27) is applied to compute estimates of plane parameters for the zero and first elevated scans ($\hat{\alpha}_1, \hat{\theta}_1, \hat{\rho}_1$), and zero and second elevated scans ($\hat{\alpha}_2, \hat{\theta}_2, \hat{\rho}_2$). Differences in plane parameter estimates are then compared to predetermined threshold values ($\delta\alpha, \delta\theta, \delta\rho$). The plane is extracted if the differences between estimates are below the thresholds, i.e. if the following conditions are satisfied:

$$\left| \hat{\alpha}_1 - \hat{\alpha}_2 \right| < \delta\alpha \ \& \ \left| \hat{\theta}_1 - \hat{\theta}_2 \right| < \delta\theta \ \& \ \left| \hat{\rho}_1 - \hat{\rho}_2 \right| < \delta\rho \qquad (28)$$

Otherwise, the plane extraction is not declared and the plane is removed from consideration. Removal of fictitious planes completes the plane reconstruction procedure.

The threshold values in equation (28) ($\delta\alpha, \delta\theta, \delta\rho$) are currently predetermined based on specifications of LADAR measurement errors. Particularly, the following threshold values are used:

$$\delta\alpha = 3 \cdot \Delta\alpha, \delta\theta = 3 \cdot \Delta\alpha, \delta\rho = 3 \cdot \sigma_\rho \qquad (29)$$

where $\Delta\alpha$ and σ_ρ are the LADAR angular resolution and standard deviation of ranging measurement noise, accordingly. The use of predetermined thresholds can be modified into an adaptive threshold choice by evaluating the real quality of lines extracted from scan images and then transforming line extraction errors into plane errors through the plane estimation equation (27). Particularly, the approach proposed in [21] exploits the actual line noise samples comprised of LADAR measurement errors and a texture of a scanned surface to estimate sigma values of line extraction errors. Hence, this approach evaluates the actual line quality and characterizes it by one-sigma values of errors in line parameter estimates (range and angle). For adaptive choice of plane extraction thresholds, line errors must be first transformed into plane parameter errors for ($\hat{\alpha}_1, \hat{\theta}_1, \hat{\rho}_1$) and ($\hat{\alpha}_2, \hat{\theta}_2, \hat{\rho}_2$). Adaptive extraction thresholds then need to accommodate combined errors in ($\hat{\alpha}_1, \hat{\theta}_1, \hat{\rho}_1$) and ($\hat{\alpha}_2, \hat{\theta}_2, \hat{\rho}_2$). Aspects of the adaptive threshold choice will be addressed by future research.

The plane extraction procedure can separate planes only if differences between plane parameters exceed the threshold values in equation (29). Thus, planar surfaces with closely located normal points are merged into a single plane. The procedure does not separate those planes that are nearly coplanar (i.e. differences in angular plane parameters are below the

threshold) and are nearly at the same distance from the origin of the LADAR body-frame (i.e. differences in plane ranges are below the threshold). This feature can limit the use of the plane extraction method proposed herein for mapping applications. However, from the navigation perspective, separation of planar surfaces that are nearly coplanar does not have a considerable influence on the observability of navigation states (position and attitude). Particularly, dilution of precision (DOP) values that characterize the influence of planar geometry on the navigation solution accuracy (see the section on the use of plane parameters for computing the navigation solution for the definition of DOP) stay practically unchanged if nearly coplanar surfaces are used separately for computing the navigation solution. Thus, this paper does not address this separation.

It must be also noted that a limited elevation scan range is used for the plane extraction method presented in this section. As a result, the method has limited application in 3D mapping: i.e. map building. For navigation applications, the plane extraction method described in this report allows for a complete reconstruction of planar surfaces that are then used to compute a 3D navigation solution.

LADAR motion during scans and between consecutive scans taken at different elevation angles can degrade the accuracy of the plane extraction procedure described in the previous section. First, LADAR motion during a single scan (i.e. motion between measuring first and last points in a scan) can distort lines observed in scan images. Second, LADAR motion between consecutive scans at different elevation angles can influence the choice of plane extraction thresholds that are applied in equation (27). This section discusses the influence of LADAR motion on the planar-based navigation.

The influence of LADAR motion during scans is evaluated below for the case of SICK LMS-200 scanning LADAR. This LADAR has a scan duration of 6.5 ms, the angular resolution of 0.5 deg and a standard deviation of the ranging noise of 1 cm. LADAR motion does not introduce considerable distortions to the scan image if the LADAR displacement and LADAR rotation over the scan duration does not exceed the ranging noise level and angular resolution, correspondingly. The following conditions must be satisfied:

$$\left| \langle \mathbf{V}_{LADAR} \rangle \right| \cdot \Delta t_{scan} < \sigma_\rho$$
$$\left| \langle \omega_{LADAR} \rangle \right| \cdot \Delta t_{scan} < \Delta \alpha \tag{30}$$

where $\left| \langle \mathbf{V}_{LADAR} \rangle \right|$ is the absolute value of the average LADAR velocity during the scanning interval, $\left| \langle \omega_{LADAR} \rangle \right|$ is the absolute value of the average LADAR rotation rate during the scan, and Δt_{scan} is the scan duration. Applying range and angular error specification of the SICK LMS-200 LADAR in equation (30) yields that the LADAR velocity must not exceed 1.5 m/s and the angular rate must not exceed 77 deg/s in order to avoid motion-related distortions of scan images. While the angular motion generally stays below this angular rate threshold for most UAV applications, the velocity threshold can be exceeded for at least some of the UAV flight scenarios.

19

LADAR scans at different elevation angles are separated by a finite time interval. If the LADAR motion between scans exceeds ranging noise and angular resolution, this motion must be taken into account. The maximum allowable translational motion and rotational motion between scans are computed as follows:

$$
\begin{aligned}
\left| \left\langle V_{LADAR} \right\rangle \right| \cdot \Delta T_{scans} &< \sigma_\rho \\
\left| \left\langle \omega_{LADAR} \right\rangle \right| \cdot \Delta T_{scans} &< \Delta \alpha
\end{aligned}
\tag{31}
$$

where ΔT_{scans} is the time interval between two consecutive scans at different elevation angles. For the current system implementation that is described in the test setup section below, ΔT_{scans} is equal to 0.7 s. In this case, the maximum allowable LADAR velocity and angular rate that does not require the use of motion compensation procedures are estimated as 1.4 cm/s and 0.7 deg/s, accordingly. For UAV operational scenarios where these motion thresholds are exceeded, INS data must be used for the LADAR motion compensation. To apply the INS-based motion compensation approach, the coordinate transformation equation (18) is modified to accommodate the LADAR motion between horizontal and elevated scans. For a general case of an arbitrary LADAR motion between these scans, equation (18) is modified as follows:

$$
\begin{bmatrix} x_b \\ y_b \\ z_b \end{bmatrix} = C_{INS} \cdot \begin{bmatrix} x_b' \\ y_b' \\ z_b' \end{bmatrix} - \begin{bmatrix} \Delta x_{INS} \\ \Delta y_{INS} \\ \Delta z_{INS} \end{bmatrix}
\tag{32}
$$

where C_{INS} is the INS estimate of the DCM for the LADAR rotation between scans (for a general case, this rotation includes both forced elevation rotation of the LADAR and any additional rotations due to the motion of autonomous vehicle), and Δx_{INS}, Δy_{INS}, and Δz_{INS} are the INS estimates of the LADAR displacement components resolved in the axes of the LADAR body frame at the horizontal scan. Taking into account equation (32), the equation for the planar surface in the tilted scan frame is modified as follows:

$$
\begin{aligned}
&x_b' \cdot \left(C_{11} \cdot \cos(\alpha) \cdot \cos(\theta) + C_{21} \cdot \sin(\alpha) \cdot \cos(\theta) + C_{31} \cdot \sin(\theta) \right) + \\
&y_b' \cdot \left(C_{12} \cdot \cos(\alpha) \cdot \cos(\theta) + C_{22} \cdot \sin(\alpha) \cdot \cos(\theta) + C_{32} \cdot \sin(\theta) \right) + \\
&z_b' \cdot \left(C_{13} \cdot \cos(\alpha) \cdot \cos(\theta) + C_{23} \cdot \sin(\alpha) \cdot \cos(\theta) + C_{33} \cdot \sin(\theta) \right) + \\
&\Delta x_{INS} \cdot \cos(\alpha) \cdot \cos(\theta) + \Delta y_{INS} \cdot \sin(\alpha) \cdot \cos(\theta) + \Delta z_{INS} \cdot \sin(\theta) = \rho
\end{aligned}
\tag{33}
$$

where $C_{k,j}$, $k=1,..3$, $j=1,..3$ are the elements of the INS direction cosine matrix C_{INS}. Accordingly, equation (20) that expresses the line extracted from the tilted scan image (i.e. for $z_b' = 0$) is modified as follows:

$$
\begin{aligned}
&x_b' \cdot \left(C_{11} \cdot \cos(\alpha) \cdot \cos(\theta) + C_{21} \cdot \sin(\alpha) \cdot \cos(\theta) + C_{31} \cdot \sin(\theta) \right) + \\
&y_b' \cdot \left(C_{12} \cdot \cos(\alpha) \cdot \cos(\theta) + C_{22} \cdot \sin(\alpha) \cdot \cos(\theta) + C_{32} \cdot \sin(\theta) \right) + \\
&\Delta x_{INS} \cdot \cos(\alpha) \cdot \cos(\theta) + \Delta y_{INS} \cdot \sin(\alpha) \cdot \cos(\theta) + \Delta z_{INS} \cdot \sin(\theta) = \rho
\end{aligned}
\tag{34}
$$

20

Similar to the derivation of equations (22) through (27), the modified plane extraction procedure was derived from equations (17), (34) and (21):

$$\hat{\alpha} = \hat{\alpha}_{line_1}$$

$$\hat{\theta} = \text{arctg}\left(\frac{1}{C_{32}\hat{\rho}_{line_2} + \Delta z_{INS}\sin(\hat{\alpha}_{line_2})} \cdot \left(\begin{array}{c} \hat{\rho}_{line_1}\sin(\hat{\alpha}_{line_2}) - \\ \hat{\rho}_{line_2}\left(C_{12}\cos(\hat{\alpha}_{line_1}) + C_{22}\sin(\hat{\alpha}_{line_1})\right) - \\ \left(\Delta x_{INS}\cos(\hat{\alpha}_{line_1}) + \Delta y_{INS}\sin(\hat{\alpha}_{line_1})\right)\sin(\hat{\alpha}_{line_2}) \end{array}\right)\right) \quad (35)$$

$$\hat{\rho} = \hat{\rho}_{line_1}\cos(\hat{\theta})$$

A modified plane extraction procedure, which uses inertial data (C_{INS}, Δx_{INS}, Δy_{INS}, and Δz_{INS}) for the LADAR motion compensation as it is formulated by equation (35), will be implemented by future development that will consider LADAR/INS integration aspects of the planar-based navigation.

3.4   Alternative Plane Reconstruction Method

Given multiple measurements made with a 2D laser scanner of the same surface as illustrated in Figure 8, we can set up a set of equations for 3D translational motion. Let us inspect the case for three measurements (at times t_0, t_1 and t_2) of a single planar surface, P, from consecutive 2D LADAR scans. Each measurement is a line segment composed of multiple scan points.

Let's define a centroid, $\mathbf{p}_0$, of the line segment at t_0:

$$\mathbf{p}_0 = \sum_{j=0}^{N_0-1}\mathbf{p}_{j,0} \quad (36)$$

where $\mathbf{p}_{j,0}$ are the 'laser' points at time t_0.

Given a rotational motion of the body from time t_0 to t_1 given by the DCM, $C_{b(t_1)}^{b(t_0)}$, a difference in orientation between the gimbaled LADAR frame between t_0 to t_1 given by the DCM, $C_{\ell_1}^{\ell_0}$, and the displacement of the LADAR reference point equal to Δx_0, the points observed on the second line segment ℓ_1, $\mathbf{p}'_{j,1}$, can expressed in the coordinate frame of ℓ_0:

$$\mathbf{p}_{j,1} = C_{t_1}^{t_0}C_{\ell_1}^{\ell_0}\mathbf{p}'_{j,1} - \Delta x_0 \ f \ or \ j = 1,...,N_1 \quad (37)$$

Note that equation (37) includes the motion compensation similar to equation (32). Now,

define vectors $\mathbf{a}_j$ from the centroid of ℓ_0 at t_0 to each of the individual points of the line segment observed at time t_1 given by:

$$\mathbf{a}_j = \mathbf{p}_{j,1} - \mathbf{p}_0 \; f \; or \; j = 1,...,N_1 \tag{38}$$

In the absence of any errors, all vectors $\mathbf{a}_j$ lie in planar surface P and should satisfy the following condition:

$$\mathbf{a}_j \cdot \mathbf{n}_P = 0 \tag{39}$$

or in matrix form using all points on the second line:

$$\mathbf{A}\mathbf{n}_P = 0 \tag{40}$$

where

$$\mathbf{A} = \begin{bmatrix} \mathbf{a}_1^T \\ \vdots \\ \mathbf{a}_{N_1}^T \end{bmatrix} \tag{41}$$

In other words, $\mathbf{n}_P$ is located in the Null-space of $\mathbf{A}$, or $\mathcal{N}(\mathbf{A})$. The eigenvectors of $\mathbf{A}^T\mathbf{A}$ associated with the zero-eigenvalues span the null-space $\mathcal{N}(\mathbf{A})$. These vectors can be obtained from the Singular Value Decomposition of $\mathbf{A}$:

$$\mathbf{A} = \mathbf{U}\mathbf{D}\mathbf{V}^T \tag{42}$$

where $\mathbf{V}$ is the matrix

$$\mathbf{V} = \begin{bmatrix} \mathbf{v}_1 & \mathbf{v}_2 & \mathbf{v}_3 \end{bmatrix} \tag{43}$$

consisting of eigenvectors of $\mathbf{A}^T\mathbf{A}$. Since the rank of $\mathbf{A}$ is 3 and only two vector are required to span the planar surface P, the third column of V corresponds to the smallest eigenvalue and is thus the best estimate of the normal to the planar surface, or:

$$\hat{\mathbf{n}}_P = \mathbf{v}_3 \tag{44}$$

The centroid of this new planar surface can thus be estimated as follows:

$$\mathbf{p}_{0,i} = \frac{1}{N_0 + N_1}\left\{ \sum_{j=0}^{N_0-1} \mathbf{p}_{j,0} + \sum_{k=0}^{N_1-1} \mathbf{p}_{k,1} \right\} \tag{45}$$

Finally, the plane range for plane 'i' can be computed by substituting (44) and (45) into equation (1):

22

$$\rho_i = \frac{1}{N_0 + N_1} \left| \left\{ \sum_{j=0}^{N_0-1} \mathbf{p}_{j,0} + \sum_{k=0}^{N_1-1} \mathbf{p}_{k,1} \right\} \mathbf{v}_3 \right| \tag{46}$$

3.5 Navigation using Planar Surfaces

Given the linear equation in (4) and the planar surface normal and distance obtained from equation (27) or (44) and (46), the translational motion of the vehicle can be solved in a standard Least Mean Squared (LMS) sense by:

$$\Delta \hat{\mathbf{x}} = \left(\mathbf{H}^T \cdot \mathbf{H} \right)^{-1} \cdot \mathbf{H}^T \cdot \Delta \hat{\rho} \tag{47}$$

In (47), $\Delta \hat{\rho}$ is the estimated delta range vector, which contains differences in estimates of plane ranges computed based on LADAR data for scans i and j.

The LMS position accuracy depends on the relative plane geometry, which is determined by the LMS measurement matrix (the **H** matrix). This paper uses Dilution of Precision (DOP) factors to characterize the geometry influence on the relationship between the localization accuracy and the planar range accuracies. DOP factors for the LMS solution defined by equation (47) are formulated in this section. The next section uses simulation results to illustrate the influence of relative planar geometry on the delta positioning accuracy.

The DOP-based approach is adopted from the Global Positioning System (GPS) where DOPs are employed to characterize the influence of satellite geometry on the positioning accuracy. Generally speaking, the use of DOP factors for plane-based localization allows evaluation of the localization accuracy for a given plane geometry and accuracy of the plane range estimates. More specifically, the DOP is defined as a geometry dependent linear coefficient that relates a standard deviation of the delta position estimation error to a standard deviation of the delta range error. For instance, a Vertical DOP (VDOP) relates a standard deviation of the vertical delta position error ($\sigma_{\Delta x_V}$) with a standard deviation of error in plane range changes ($\sigma_{\Delta \rho}$):

$$\sigma_{\Delta x_V} = \text{VDOP} \cdot \sigma_{?\rho} \tag{48}$$

Dilution of Precision (DOP) factors can be formulated for the plane based navigation similarly to the GPS DOP formulation (see reference [22] for the corresponding formulation of GPS DOPs). From equation (47) it follows that the relationship between the position error vector ($\delta(\Delta \mathbf{x})$) and the range change error vector ($\delta(\Delta \rho)$) is given by:

$$\delta(\Delta \mathbf{x}) = \left(\mathbf{H}^T \cdot \mathbf{H} \right)^{-1} \cdot \mathbf{H}^T \cdot \delta(\Delta \rho) \tag{49}$$

23

The variance of $\delta(\Delta R)$ is derived from equation (49) and yields the following variance relation:

$$\mathbf{VAR}_{\delta(\Delta x)} = \left(\mathbf{H}^T \cdot \mathbf{H}\right)^{-1} \cdot \mathbf{H}^T \cdot \mathbf{VAR}_{\delta(\Delta\rho)} \cdot \mathbf{H} \cdot \left(\mathbf{H}^T \cdot \mathbf{H}\right)^{-1} \tag{50}$$

where:

$$\mathbf{VAR}_x = E[\mathbf{x} \cdot \mathbf{x}^T] \tag{51}$$

and E[.] is the expected value. If the components of $\delta(\Delta\rho)$ are assumed to be independent and identically distributed (i.i.d.), then

$$\mathbf{VAR}_{\delta(\Delta\rho)} - \mathbf{I} \cdot \sigma_{\Delta\rho} \tag{52}$$

where $\mathbf{I}$ is a unit matrix and $\sigma_{\Delta\rho}$ is the standard deviation of the delta range error. Substitution of equation (52) into equation (50) yields:

$$\mathbf{VAR}_{\delta(\Delta x)} = \left(\mathbf{H}^T \cdot \mathbf{H}\right)^{-1} \cdot \sigma_{\Delta\rho}^2 \tag{53}$$

DOP factors are thus formulated as follows:

$$\mathbf{D} = \sqrt{\left(\mathbf{H}^T \cdot \mathbf{H}\right)^{-1}} \tag{54}$$

where xDOP = $[\mathbf{D}]_{11}$, yDOP = $[\mathbf{D}]_{22}$ and zDOP = $[\mathbf{D}]_{33}$, correspondingly. As mentioned previously, equation (54) is derived assuming that range errors for different planar surfaces are identically distributed and uncorrelated with each other. The non-correlation assumption is generally valid since different planes are computed from different LADAR measurements that are normally uncorrelated and computation of plane parameters for different planes is completely separate. However, range errors associated with ranges to different planes can have different standard deviation values. In this case, the un-weighted LMS estimation (see equation (47)) must be modified to a weighted LMS solution procedure. DOP formulation for a weighted LMS solution is recommended as a topic for future research.

Let's come back to finding $\mathbf{C}_{b(t_k)}^{b(t_{k+1})}$ in equation (7) from the observed normal vectors. To compute the DCM, the attitude estimation algorithm needs to solve Wahba's problem [23]: given a first set of normal vectors with vector components resolved at the i-scan's frame and the second set of the same vectors with their components resolved at the j-scan's frame, find the DCM that brings the second set into the best least square correspondence with the first. At least two non-collinear normal vectors are required for the attitude estimation. Attitude is generally estimated by solving an eigenvalue/eigenvector problem, which requires solution of non-linear equations. For instance, the quaternion estimation algorithm (QUEST) finds the optimal LMS quaternion by computing eigenvalues and

24

eigenvectors of a four-by-four Hessian matrix [24]. In this case, a fourth order equation has to be solved in order to computer eigenvalues. This paper implements a two-step attitude estimation approach. First, an initial (non-optimal) DCM is computed based on two non-collinear normal vectors. Second, DCM initialization errors are optimally estimated by applying a standard linear LMS formulation. The use of linear solution vs. non-linear solution techniques is beneficial for error analysis, since it allows for a direct transformation of plane extraction errors into attitude estimation errors. The two-step attitude estimation procedure is discussed next.

As stated previously, the DCM is first initialized based on two non-collinear vectors. Initial DCM is found based on two computational rotations of the j-frame that align j-frame vector components with their components at the i-frame. Corresponding DCM computations are described in details in [25]. Main computational steps are summarized below. Two associated non-collinear plane vectors extracted from scan i and scan j ($\hat{n}_{i,k_0}$, $\hat{n}_{i,m_0}$ and $\hat{n}_{j,k_0}$, $\hat{n}_{j,m_0}$) are used to compute the initial DCM. Two vectors with the maximum absolute value of their cross product are chosen amongst all available plane normal vectors to maximize non-collinearity. An extensive search is performed through all possible pairs of normal vectors extracted from scan i to find the vector pair that maximizes the cross-product absolute value:

$$\left| \hat{n}_{i,k_0} \times \hat{n}_{i,m_0} \right| = \max_{\substack{k=1,\dots,M \\ m=1,\dots,M}} \left| \hat{n}_{i,k} \times \hat{n}_{i,m} \right| \qquad (55)$$

where $\times$ is the vector cross-product and M is the total number of planes extracted.

As stated above, the DCM is computed based on two computational rotations of the j-frame that match j-frame vectors components $\hat{n}_{j,k_0}$ and $\hat{n}_{j,m_0}$ with their i-frame components $\hat{n}_{i,k_0}$ and $\hat{n}_{i,m_0}$. First rotation matches components of $\hat{n}_{j,k_0}$ and $\hat{n}_{i,k_0}$: i.e., the j-frame is computationally rotated such that $\hat{n}_{j,k_0}$ vector components become $\hat{n}_{i,k_0}$ components at the end of rotation as illustrated in Figure 13.
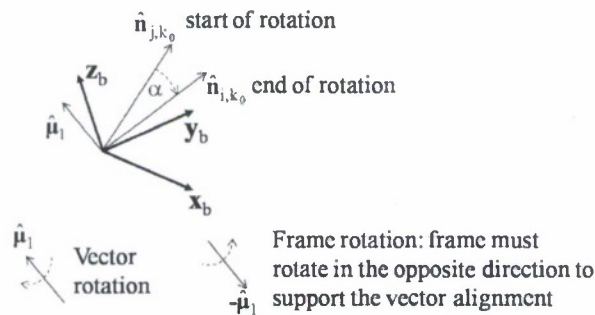

Figure 13. Computational rotation of j-frame that aligns vector components at j-frame with its components at i-frame

25

Hence, $\hat{n}_{j,k_0}$ is rotated relative to the j-frame as shown in Figure 13. The rotation axis $\hat{\mu}_1$ is perpendicular to both $\hat{n}_{i,k_0}$ and $\hat{n}_{j,m_0}$, i.e.:

$$\hat{\mu}_1 = \hat{n}_{i,k_0} \times \hat{n}_{j,k_0} \tag{56}$$

and the rotation angle ϕ_1 is the angle between $\hat{n}_{i,k_0}$ and $\hat{n}_{j,k_0}$:

$$\phi_1 = \arccos\left(\hat{n}_{j,k_0} \cdot \hat{n}_{i,k_0}\right) \tag{57}$$

To support this vector rotation, j-frame must be rotated in the direction opposite to the vector rotation. Thus, based on rotation angle and rotation axis, the DCM of the first rotation is computed as follows:

$$\hat{C}_1 = \text{expm}\left(\phi_1 \cdot \hat{\mu}_1 \times\right) \tag{58}$$

where '*expm*' is the exponential matrix function and $\hat{\mu}_1 \times$ is the skew-symmetric matrix defined as follows:

$$\hat{\mu}_1 \times = \begin{bmatrix} 0 & -\hat{\mu}_{1z} & \hat{\mu}_{1y} \\ \hat{\mu}_{1z} & 0 & -\hat{\mu}_{1x} \\ -\hat{\mu}_{1y} & \hat{\mu}_{1x} & 0 \end{bmatrix} \tag{59}$$

After the first rotation, the following condition is satisfied:

$$\hat{n}_{i,k_0} = \hat{C}_1 \cdot \hat{n}_{j,k_0} \tag{60}$$

and, components of the second normal vector are transformed as follows:

$$\hat{n}'_{j,m_0} = \hat{C}_1 \cdot \hat{n}_{j,m_0} \tag{61}$$

The second rotation matches $\hat{n}'_{j,m_0}$ with $\hat{n}_{i,m_0}$ while previously matched $\hat{n}_{i,k_0}$ and $\hat{n}_{j,k_0}$ remain unchanged:

$$\hat{n}_{i,m_0} = \hat{C}_2 \cdot \hat{n}'_{j,m_0} ; \quad \hat{C}_2 \cdot \hat{n}_{i,k_0} = \hat{n}_{i,k_0} \tag{62}$$

Correspondingly, $\hat{n}_{i,k_0}$ serves as a rotation axis for the second rotation (i.e. $\hat{\mu}_2 = \hat{n}_{i,k_0}$). The rotation angle is chosen to satisfy the first condition in equation (62). In this case, the rotation angle ϕ_2 can be estimated as the angle between projections of $\hat{n}'_{j,m_0}$ and $\hat{n}_{i,m_0}$ on the planar surface perpendicular to $\hat{n}_{i,k_0}$ (see [25] for more details). Computation of the DCM for the second rotation is similar to DCM computations for the first rotation:

$$\hat{C}_2 = \text{expm}\left(\hat{\phi}_2 \cdot \hat{\mu}_2 \times\right) \tag{63}$$

The initial DCM estimate is determined as a superposition of the above rotations:

$$\left(\hat{C}_j^i\right)_0 = \hat{C}_2 \cdot \hat{C}_1 \tag{64}$$

The initial estimate of the direction cosine matrix can be represented as follows:

$$\left(\hat{C}_j^i\right)_0 = \delta C_j^i \cdot C_j^i \tag{65}$$

where δC_i^j is the DCM estimation error matrix. Linear approximation of this matrix yields:

$$\delta C_j^i \approx I + \delta\Omega \times \tag{66}$$

where $\delta\Omega \times$ is the skew-symmetric matrix:

$$\delta\Omega\times = \begin{bmatrix} 0 & -\delta\psi & \delta\theta \\ \delta\psi & 0 & -\delta\phi \\ -\delta\theta & \delta\phi & 0 \end{bmatrix} \tag{67}$$

and $\delta\theta$, $\delta\phi$, and $\delta\psi$ are errors in pitch, roll, and heading angles after the DCM initialization stage. The second stage of the DCM estimation procedure implements a linear LMS solution to estimate these angular errors. This LMS solution procedure is discussed below.

Substitution of equation (66) into equation (65) provides the following expression:

$$\left(\hat{C}_j^i\right)_0 = \delta C_j^i \cdot C_j^i \approx \left(I + \delta\times\right) \cdot C_j^i = C_j^i + \delta\times \cdot C_j^i \tag{68}$$

Correspondingly:

$$\begin{aligned} \left(\hat{C}_j^i\right)_0 \cdot n_j - n_i &= \left(I + \delta\times\right) \cdot C_j^i \cdot n_j - n_i = \left(I + \delta\times\right) \cdot n_i - n_i \\ &= n_i + \left(\delta\times\right) \cdot n_i - n_i = \delta \times n_i = -n_i \times \delta \end{aligned} \tag{69}$$

Note that Equation (69) uses equivalency of the matrix multiplication $\left(\delta\Omega\times\right) \cdot n_i$ to the vector cross-product $\delta\Omega \times n_i$. Expanding equation (69) to include all available normal vectors yields:

$$\Delta n = H_\Omega^T \cdot \delta\Omega \tag{70}$$

where:

$$\Delta n = \begin{bmatrix} \left(\hat{C}_i^j\right)_0 \cdot n_{i,1} - n_{j,1} \\ \dots \\ \left(\hat{C}_i^j\right)_0 \cdot n_{i,M} - n_{j,M} \end{bmatrix}, H_\Omega = \begin{bmatrix} -n_{j,1} \times \\ \dots \\ -n_{j,M} \times \end{bmatrix} \tag{71}$$

A LMS solution is applied to estimate initial angular errors:

$$\delta\hat{\Omega} = \left(H_\Omega^T \cdot H_\Omega\right)^1 \cdot H_\Omega^T \cdot \Delta\hat{n} \tag{72}$$

Note that the measurement matrix $\Delta\hat{n}$ is based on estimated values of plane normal vectors that are computed from LADAR data. Finally, the initial DCM estimate is adjusted to incorporate LMS estimates of initial angular errors:

$$\hat{C}_j^i = \text{expm}\left(-\delta\hat{\Omega}\times\right)\left(\hat{C}_j^i\right)_0 \tag{73}$$

Equation (72) provides the linear relation between plane normal vectors and angular adjustments. Unlike non-linear attitude estimation methods, this linear relation can be directly applied to formulate the influence of relative plane geometry on the estimation accuracy of the LADAR platform pitch, roll, and heading angles. Similarly to the delta position LMS solution above, DOP factors can be derived to relate errors in plane normal vectors to angular errors. However, unlike the range errors for the position case, the normal vector errors are generally correlated. Particularly, errors in components of the same normal vector are correlated as it can be inferred from equations (10) and (37). This correlation needs to be taken into account for the derivation of DOP factors for the attitude case. This derivation is outside the scope of this report.

In order to use planar surfaces for the estimation of position and orientation changes as formulated in this section, it must be known with certainty that a plane in scan i corresponds to the plane in scan j. For plane matching, INS data can be used to predict the plane range and normal vector in scan j based on range and normal vector extracted from scan i:

$$\hat{\rho}_j^- = \hat{\rho}_i - \left(\Delta\hat{x}_{INS}, n_i\right)$$
$$\hat{n}_j^- = \Delta\hat{C}_{INS} \cdot \hat{n}_i \tag{74}$$

where $\hat{\rho}_j^-$ and $\hat{n}_j^-$ are predicted range and normal vector; $\hat{\rho}_i$ and $\hat{n}_i$ are plane range and normal vector extracted from scan i; and, $\Delta\hat{x}_{INS}$ and $\Delta\hat{C}_{INS}$ are the INS estimates of the position change vector and direction cosine matrix increment between scans i and j. If the predicted range and normal vector ($\hat{\rho}_j^-$ and $\hat{n}_j^-$) match closely to the range and normal vector extracted from scan j ($\hat{\rho}_j$ and $\hat{n}_j$), the plane correspondence is established between

28

scans i and j. Note that plane matching thresholds must accommodate both plane extraction errors and INS drift errors. As stated previously, implementation of the feature matching procedure that exploits inertial data will be addressed by future research. For the current realization of the 3D navigation solution, simulation and test scenarios are designed such that a direct plane correspondence can be used to match planes between different scans: i.e., a kth plane extracted from scan i always correspond to the kth plane extracted from scan j.

3.6 Simulation Results

The plane-based navigation methodology is first verified using simulations. Three planar surfaces are simulated according to the geometry shown in Figure 14.
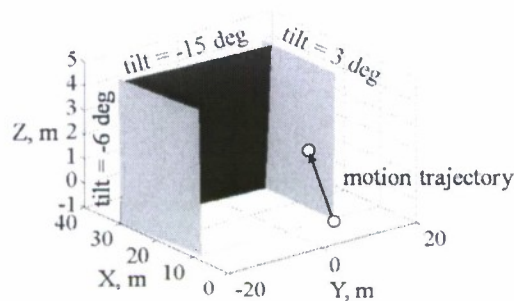
Figure 14. Simulation scenario for the 3D plane-based navigation: three planar surfaces are simulated

For this planar geometry, DOP factors for the position estimation are computed as 0.7, 3.1, and 10.6 for the xDOP, yDOP and zDOP, respectively. 2D LADAR scans are simulated at 0 deg, 5 deg, and 10 deg elevation angles. The simulated LADAR measurements conform to the specifications of a SICK LMS-200 LADAR. The LADAR angular range is from 0 to 180 deg with the angular resolution of 0.5 deg. The LADAR distance range is from 0 to 80 m with a 1 cm ranging noise standard deviation.

The translational motion trajectory is simulated as a constant velocity motion from the start to the end trajectory points. Simultaneous rotations of the LADAR about the x, y, and z axes of the LADAR body frame are simulated with rotation rate of 0.2 deg per 3D scan, 0.25 deg per 3D scan, and 0.3 deg per 3D scan, correspondingly. Note that one 3D scan corresponds to three consecutive 2D scans at 0 deg, 5 deg, and 10 deg elevation angles. Six motion components (three translational motion components and three rotational motion components) are thus implemented for the simulation test. Axes of the LADAR body frame coincide with the navigation frame axes (x, y, z axes in Figure 12) at the initial time (start of the trajectory).

Delta position and delta orientation estimates are computed based on changes in plane parameters between the initial 3D scan and the current 3D scan. Thus, delta position and orientation estimates correspond to position and orientation changes between the start of the trajectory and the current trajectory point.

29

Figure 15 shows errors in delta position estimate. Delta position errors herein are computed as the differences between the delta position vector derived from LADAR measurements and the true delta position vector. Delta position errors are at the cm level with one sigma values estimated as 0.5 cm, 2.3 cm, and 8.4 cm for x, y and z delta position error components, accordingly. Note that the ratio of xDOP, yDOP, and zDOP values (0.7:3.1:10.6) closely reflects the ratio of delta position sigma values (0.5:2.3:8.4).
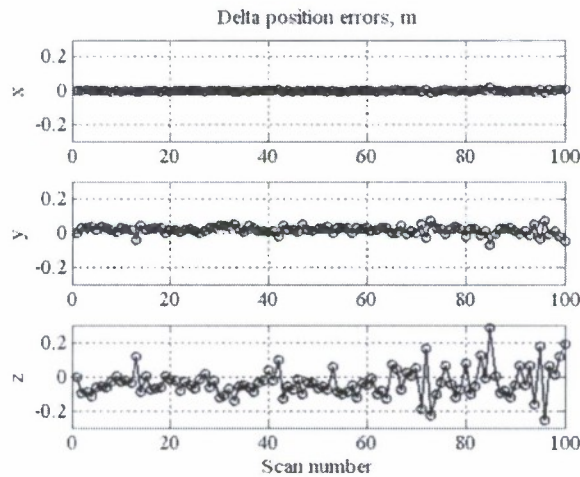

Figure 15. 3D plane-based navigation: delta position errors of the 3D navigation solution

Figure 16 shows errors in angular estimates. To compare the computed attitude with the reference attitude trajectory, the estimated DCM was transformed into Euler angles (pitch, roll and heading) using a standard transformation routine described in [26].
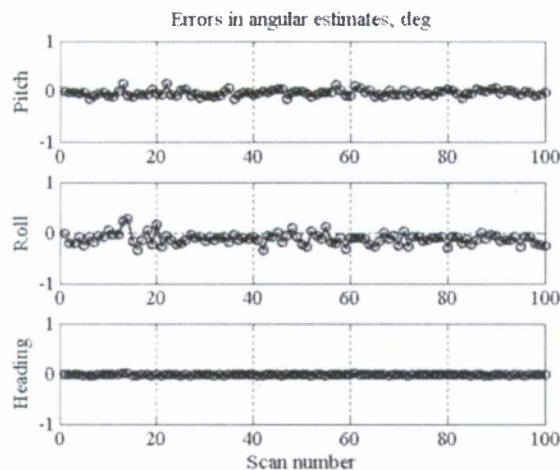
Figure 16. 3D plane-based navigation: angular errors of the 3D planar-based navigation solution

30

Standard deviations of errors in pitch, roll and heading estimates are computed as 0.07 deg, 0.1 deg, and 0.01 deg, respectively.

To illustrate the influence of the plane geometry on the delta position accuracy, the tilt angle of one of the simulated planes is increased from 3 deg to 30 deg as shown in Figure 17. As a result, the VDOP value is decreased from 10.6 to 2.3.
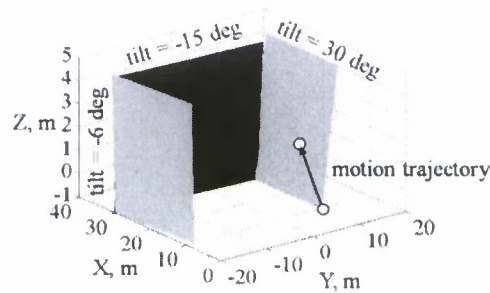

Figure 17. 3D plane-based navigation (Scenario 2): three planar surfaces are simulated, tilt angle of one of the planes is increased to 30 deg to improve the VDOP factor

Figure 18 shows the corresponding delta position error plots. Accordingly, the standard deviation of the z delta position error is decreased from 8.4 cm to 2.2 cm as a result of the VDOP decrease.
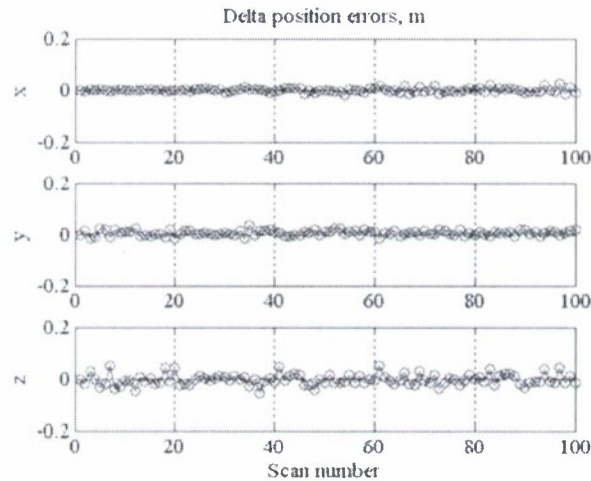
Figure 18. 3D plane-based navigation (Scenario 2): errors in the delta position solution

The simulation scenarios implemented above demonstrate that non-vertical planes are required to observe changes in the z position component. For applications such as autonomous operation of UAVs in urban environments, this requirement may not always be satisfied, particularly, for those cases where planar surfaces are created by vertical walls of surrounding buildings. In these cases, the system can be augmented by a downward-looking scanning LADAR capable of extracting the horizontal planar surfaces created, for instance, by urban roads.

31

3.7 Test Setup and Results

Figure 19 shows a photograph of the test setup that is developed to demonstrate the feasibility of 3D trajectory estimation from LADAR measurements.
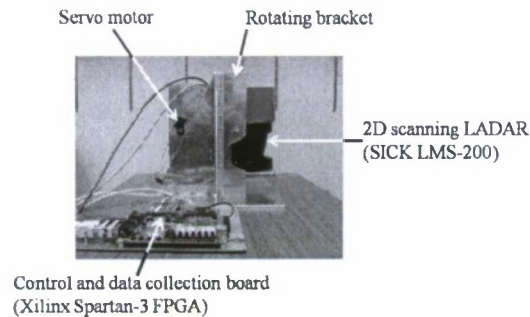

Figure 19. Photograph of the test setup: the setup includes a scanning LADAR, rotating bracket, a low-cost servo motor, and an FPGA-based control and data collection board

A SICK LMS-200 2D scanning LADAR is mounted in a bracket that is capable of rotating around the x axis of the LADAR body frame. LADAR rotations are implemented using a low-cost Futaba digital servo motor. Scans are taken at elevation angles of 0 deg, 5 deg and 10 deg. The servo control and LADAR data collection functions are implemented in a Xilinx Spartan 3 Field Programmable Gate Arrays (FPGA). Figure 20 shows the diagram of the data collection setup.
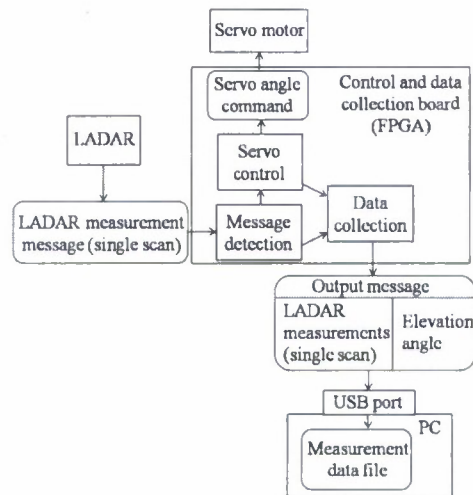
Figure 20. Diagram of the data collection setup: the FPGA-based data collection system detects a LADAR measurement message, controls servo angular position (elevation angle), includes the current value of the elevation angle into the message, and sends the updated message to a PC where measurement messages are collected for post-processing

The scanning LADAR outputs measurement messages comprising of all measurements corresponding to a single scan. LADAR messages are detected by the message detection block of the FPGA-based control and data collection board. Once the LADAR message is detected, the board updates the servo elevation angle through the servo control block. One of the key requirements for the setup design is that the LADAR motion between different elevation angles does not interfere with the LADAR scans themselves. In other words, the servo motor must change the LADAR elevation angle between scans and not during the scans to avoid introducing distortions into the scan images. To satisfy this requirement, the FPGA-based control board sends the elevation angle change command to the servo motor immediately after the detection of the LADAR measurement message. Thus, the servo has enough time to change the LADAR elevation angle before the next scan is performed. A 2D scan repetition rate of about 0.7 s is implemented for the test setup. This time interval is sufficient to change the LADAR elevation angle for the low-cost servo option used in the setup. The data collection block forms output messages where each message contains scanning measurements from a single scan and the values of the scan's elevation angle that is provided by the servo control block. Output messages are received through a USB port and stored into a binary file on a PC.

To process the experimental data, a data segmentation scheme is implemented as illustrated in Figure 21.
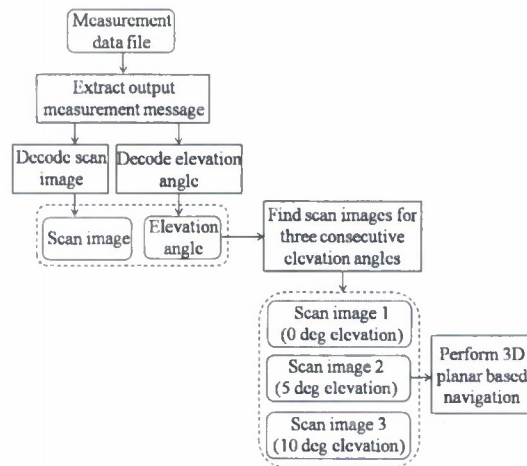

Figure 21. Segmentation of LADAR measurements from the data file: first, output measurement messages are extracted from the file; second, scan image and its corresponding elevation angle are decoded from each message; third, groups of three consecutive images (0 deg, 5 deg, and 10 deg elevation angles) are formed

Measurement messages in the data file are identified by the message header and extracted from the file. The scan image and the scan's elevation angle are decoded from each message extracted. Scan images that correspond to three consecutive elevation angles (0 deg, 5 deg, and 10 deg) are formed into groups of 2D scans. Groups of three consecutive scan images are then processed to extract planar surfaces and estimate LADAR position and orientation changes as discussed previously in the paper.

33

Results of live data tests are used to demonstrate the feasibility of the methods developed in this paper. Test scenarios are designed to demonstrate: 1) reconstruction of planar surfaces from LADAR data, and 2) estimation of position and orientation changes of the LADAR based on the extracted planar surface parameters.

Figure 22 shows a photograph of the test scene for the first live data test scenario used to demonstrate the plane reconstruction. The scans are taken in an indoor office environment. Note that the LADAR scan that corresponds to the zero elevation angle is a 2D horizontal scan.
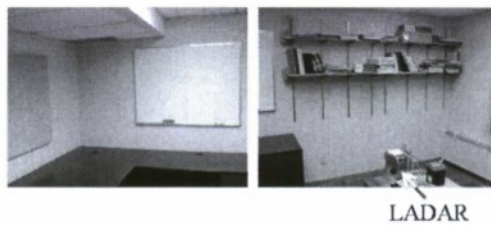

LADAR

Figure 22. Plane reconstruction based on LADAR data: photograph of the live data test scenario 1

Figure 23 shows the three planes reconstructed from the scan images. Three planes associated with the office walls in the LADAR FoV are successfully reconstructed from live LADAR data.
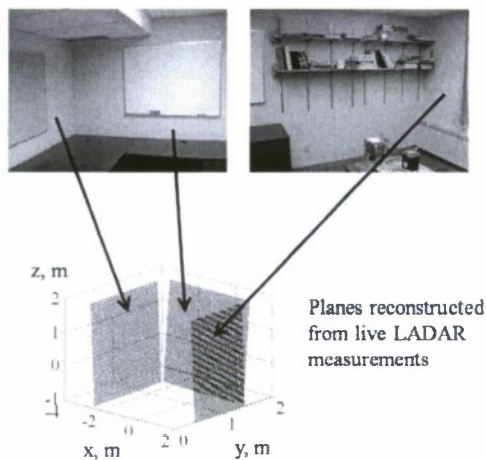

Figure 23. Reconstructed planes for the test scenario 1: planes associated with the walls in the LADAR FoV are successfully reconstructed

Two wooden boards were added to the environment for the second test scenario as illustrated in Figure 24.
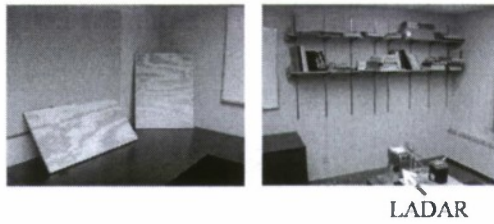
Figure 24. Plane reconstruction: photograph of the live data test scenario 2

Plane reconstruction results are shown in Figure 25 and demonstrate a successful reconstruction of planar surfaces visible to the LADAR.
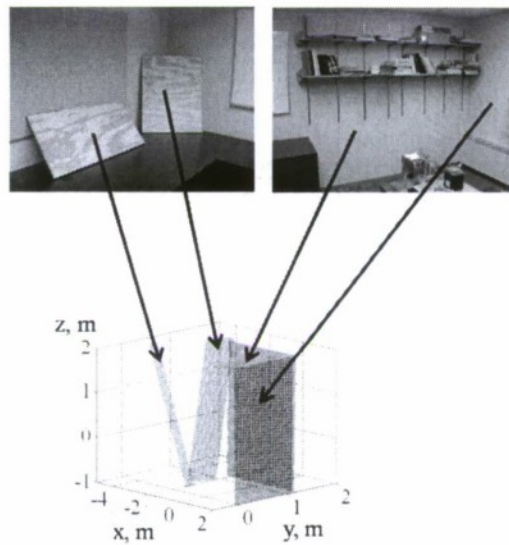

Figure 25. Reconstructed planes for the test scenario 2: two planes associated with the wooden boards as well two planes associated with office walls are successfully reconstructed; the third office wall is not visible to the LADAR as it is being blocked by the wooden boards

Feasibility of the planar-based navigation methods presented in this report was initially verified with experimental data. As mentioned previously, this report does not address LADAR/INS integration aspects of the generic 3D navigation scheme. Hence, the test scenario was designed such that INS-related procedures (motion compensation and feature matching) do not have to be applied. Particularly, the test was performed in the office environment shown in Figure 24. In this case, a direct correspondence between planes observed at different scan images can be used for feature matching (i.e., a kth plane in one image always corresponds to the kth plane in another image). In addition, the test scenario implemented does not require compensation of LADAR motion during 3D scans where a 3D scan is defined as three consecutive 2D scans at 0 deg, 5 deg, and 10 deg elevation angles. For this test scenario, stationary LADAR data were first collected for thirty 3D scans. A 3D LADAR motion was then applied: the LADAR was displaced simultaneously in x, y, and z directions (0.2 m, 0.95 m, and -0.25 m displacements, accordingly) with

simultaneous roll and heading rotations (-15 deg and 45 deg, accordingly). Following the LADAR motion, another thirty stationary scans were collected.

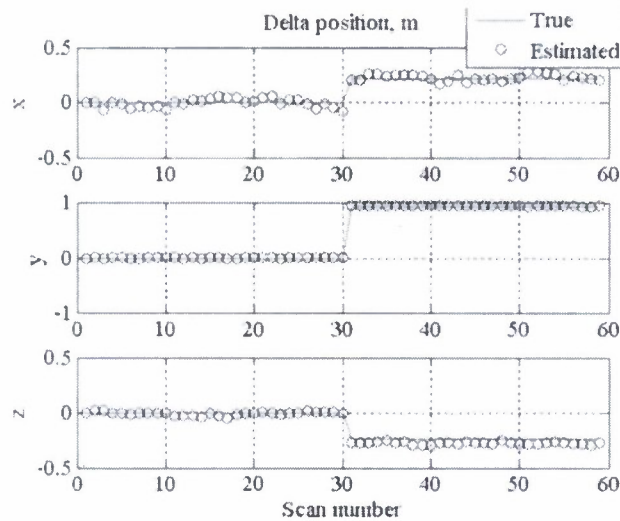Figure 26 compares delta position estimates computed from LADAR data with the true delta position.

Figure 26. Reconstruction of 3D translational motion: true trajectory vs. motion trajectory estimated by the 3D planar based navigation that uses LADAR data
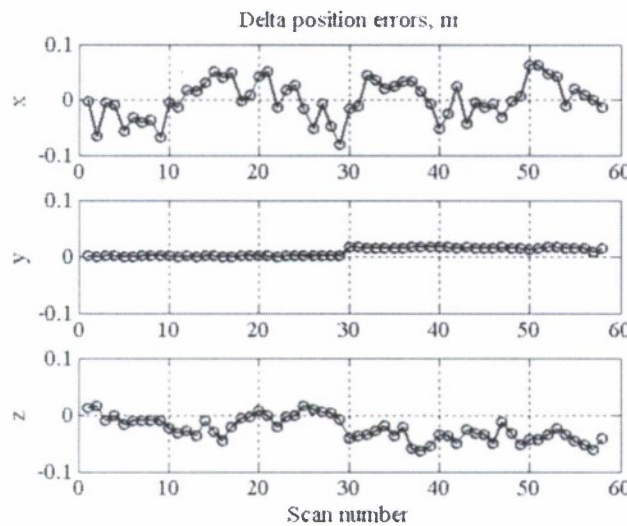
Figure 27 shows delta position errors.

Figure 27. Reconstruction of 3D translational motion: errors in delta position estimates that are computed from LADAR data

Position errors shown are at a cm-level. Standard deviations of errors in x, y, and z position components are computed as 3.5 cm, 0.7 cm, and 2.1 cm, respectively.

36

Figure 28 compares estimated rotation angles with the true attitude trajectory. Similar to the simulation scenario, DCM estimates were converted into Euler angles using standard computations.
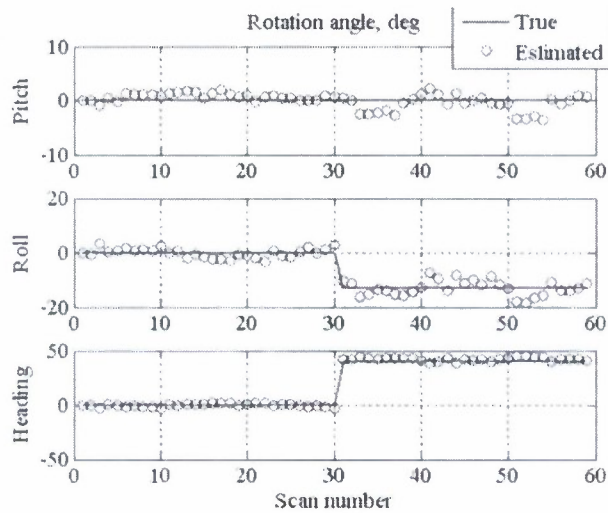

Figure 28. Reconstruction of 3D angular motion: true attitude trajectory vs. attitude estimated based on plane parameters extracted from LADAR data

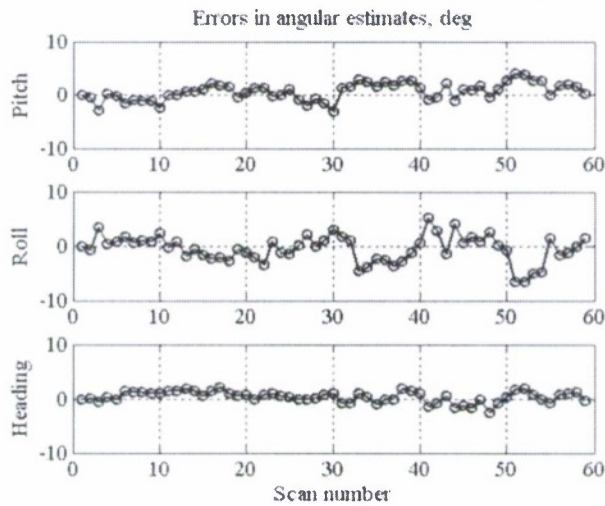Figure 29 represents angular error plots.

Figure 29. Reconstruction of 3D angular motion: errors in angular estimates of the 3D planar based navigation that uses LADAR data

Standard deviation of errors in pitch, roll, and heading angles are estimated as 1.6 deg, 2.5 deg, and 1 deg, correspondingly. It is noted that attitude errors for the live data test are increased notably as compared to attitude errors for the simulation test: the increase is from a sub-degree level to a degree level. This error increase is mainly attributed to the deviation of the actual elevation angle of the low-cost servomotor from the commanded angular value that is used for plane computations (see equation (37) above).

37

Overall, test results presented in this section proof the validity of the methodology developed to reconstruct translational motion in three dimensions at the cm accuracy level and to reconstruct rotational motion in three dimensions at the degree accuracy level. This accuracy level can be enhanced by improving the precision of the LADAR elevation rotations or by measuring these rotations precisely with the INS.

3.8 Covariance Analysis and Integrity Monitoring

The first task of integrity monitoring in 3D LADAR navigation is to detect moving objects or features from the position solution.

Moving features can be isolated and removed through monitoring of the LMS position solution residuals. It is a similar process to the moving line detection algorithm of 2D LADAR navigation, which has been accomplished in year 1. LMS residuals, as shown in (6), contain measurement error ε, which contains noise ν and bias $\mathbf{b}$.

$$\varepsilon = \nu + \mathbf{b} \tag{75}$$

$$\mathbf{e} = Q_L^T \Delta\rho = Q_L^T \varepsilon = Q_L^T (\nu + \mathbf{b}) \tag{76}$$

The measurement noise component can be attributed to the laser ranging noise and variations due to the texture of the scanned surface. The bias, however, is induced by making range measurements of a moving feature. The moving feature can be isolated by bias detection in the residual error vector. The residuals are compared against a failure detection threshold C that is determined by the desired probability of false alarm (P_{FA}) and probability of missed detection (P_{MD}). If this threshold is exceeded, a moving feature will be detected and removed from the solution. A maximum undetectable feature velocity is directly related to the minimum detectable bias (MDB) in the parity domain. If feature motion creates a solution bias that is transformed into parity bias that exceeds the MDB, this motion will be detected with given P_{FA} and P_{MD}. If the measurement noise ν is Gaussian distributed, the detection thresholds and the MDB value are defined as follows:

$$
\begin{aligned}
C_k &= \gamma \cdot \sqrt{COV^e_{(k,k)}} \\
MDB^e_k &= \beta \cdot \sqrt{COV^e_{(k,k)}} \\
k &= 1,\dots, M-3
\end{aligned}
\tag{77}
$$

where C_k is the detection threshold for the kth element of the residual vector e, MDB^e_k is the MDB for the kth element of the residual vector, and $COV^e_{(k,k)}$ is the kth row, k^{th} column element of the residual covariance. With a total of M features, at least 3 features are necessary to solve for a 3-D solution. As a result, k can be as large as M-3. It was

38

empirically decided that with $P_{FA} = 10^{-5}$, and $P_{MD} = 10^{-5}$ the scale factors are given by $\gamma=4.4$ and $\beta=7.7$.

To determine the maximum undetectable feature velocity, residual domain MDBs are transformed into the range-domain MDB. Let $Q^e = Q_L^T$ and $q_{i,j}^e$ be the element at i^{th} row and j^{th} column. If the lth measurement is associated with a moving feature, the feature motion introduces a measurement bias b, which is, in turn, transformed to the residuals according to:

$$e_1 = q_{1,J}^e \cdot b$$
$$\dots \tag{78}$$
$$e_{M-3} = q_{(M-3),J}^{(c)} \cdot b$$

The measurement bias is detected if it transforms into a parity residual that exceeds the parity-domain MDB for at least one element of the parity vector, i.e:

$$MDB_l^{(range)} = \min\left[\frac{MDB_l^e}{q_{1,J}^e}, \dots, \frac{MDB_l^e}{q_{M-3,J}^e}\right] \tag{79}$$

where $MDB_l^{(range)}$ is the measurement MDB (or, equivalently, range-domain MDB) for the lth feature. The range-domain MDB is directly related to the minimum feature velocity that can be detected by the parity test (or, equivalently, maximum feature velocity that remains undetected). Particularly, the range bias caused by feature motion is determined as follows:

$$b = V \cdot T_{exp} \tag{80}$$

where V is the average velocity in the direction perpendicular to the line associated with moving feature, and T_{exp} is the feature exposure time or feature observation interval. The maximum undetectable velocity of a feature given a fixed T_{exp}, or minimum exposure time required to detect the moving feature given the velocity can be determined using (80).

Estimation of the detection threshold and MDB using (77) relies on the covariance matrix of the LMS parity. The covariance analysis is performed based on the plane reconstruction method introduced in 3.4, by equations (36) through (46), as these equations are formed in a linear manner.

Assuming that noise of all the M scans is independent, the line measurement errors are transformed into parity error covariance as follows:

$$COV^e = Q^e \cdot COV_\rho \cdot (Q^e)^T \tag{81}$$

In equation (81) the measurement covariance is given by:

$$\mathbf{COV}_\rho = \mathrm{diag}(\sigma^2_{\rho i,(1)} + \sigma^2_{\rho j,(1)}, \sigma^2_{\rho i,(2)} + \sigma^2_{\rho j,(2)}, \ldots, \sigma^2_{\rho i,(M)} + \sigma^2_{\rho j,(M)}) \tag{82}$$

where $\sigma^2_{\rho i,l}$ and $\sigma^2_{\rho j,l}$ stand for variance of distances to l^{th} plane at the ith and j^{th} scan respectively.

As shown in equations (44) and (46),

$$\rho_i = \frac{1}{N_0 + N_1} \left| \left\{ \left(\sum_{j=0}^{N_0-1} \mathbf{p}_{j,0} + \sum_{k=0}^{N_1-1} \mathbf{p}_{k,1} \right) \cdot (\hat{\mathbf{n}}_{Pj}) \right\} \right|,$$

and, therefore,

$$
\begin{aligned}
\delta(\rho_i) &= \frac{1}{N_0 + N_1} \delta\left[\left\{ \left(\sum_{j=0}^{N_0-1} \mathbf{p}_{j,0} + \sum_{k=0}^{N_1-1} \mathbf{p}_{k,1} \right) \right\} \cdot (\hat{\mathbf{n}}_{Pj}) \right] \\
&+ \frac{1}{N_0 + N_1} \left\{ \sum_{j=0}^{N_0-1} \mathbf{p}_{j,0} + \sum_{k=0}^{N_1-1} \mathbf{p}_{k,1} \right\} \delta[\hat{\mathbf{n}}_{Pj}]
\end{aligned}
\tag{83}
$$

Whereas, the first component in equation (83) represents the error directly associated with the LADAR point observables, the second component describes the error caused by inaccurate normal vector estimation. Although the two components are not independent from each other, they are conservatively modeled as uncorrelated error sources.

The term $\dfrac{1}{N_0 + N_1} \delta\left[\left\{ \left(\sum_{j=0}^{N_0-1} \mathbf{p}_{j,0} + \sum_{k=0}^{N_1-1} \mathbf{p}_{k,1} \right) \right\} \right]$ represents the average measurement error of

all the laser points on both line segments. The measurement error of each individual laser point can be estimated with:

$$\sigma^2 \leq \sigma^2_{LS} + \sigma^2_{texture} \tag{84}$$

where σ_{LS} is the standard deviation of range measurement noise and $\sigma_{texture}$ represents the error due to the texture of a scanned object. As a result, the variance of the first component of (83) can be over-bounded by:

$$\frac{1}{N_0 + N_1} \delta\left[\left\{ \left(\sum_{j=0}^{N_0-1} \mathbf{p}_{j,0} + \sum_{k=0}^{N_1-1} \mathbf{p}_{k,1} \right) \right\} \right] \cdot (\hat{\mathbf{n}}_P) \leq \frac{1}{N_0 + N_1} \sigma^2 \tag{85}$$

Variance estimation of the second component in (83) requires knowledge of the error in the normal vector of the planar surface P, $\mathbf{n}_P$. As defined in (38) and (39), with the centroid of line segment ℓ_0, $\mathbf{p}_0$, and an arbitrary point on ℓ_1, $\mathbf{p}_{j,1}$, the normal vector of the plane has

to satisfy $(\mathbf{p}_{j,1} - \mathbf{p}_0) \cdot \mathbf{n}_P = 0$. Therefore, the measurement noise on $\mathbf{p}_0$ and $\mathbf{p}_{j,1}$ is transformed into noise on the normal vector using

$$\delta \mathbf{n}_{P,j} = \frac{\delta(\mathbf{p}_0) - \delta(\mathbf{p}_{j,1})}{\left| \mathbf{p}_{j,1} - \mathbf{p}_0 \right|} \tag{86}$$

where $\delta \mathbf{n}_{P,j}$ is the error on $\mathbf{n}_P$ contributed by $\mathbf{p}_0$ and $\mathbf{p}_{j,1}$.

For simplicity of analysis, we assume that the noise components of $\mathbf{p}_0$, $\mathbf{p}_{j,1}$ and $\mathbf{n}_P$ are independent on x y and z directions. Future research included in Year 3 of this effort will verify these assumptions. As a the three covariance matrices are approximated by:

$$\text{cov}(\delta \mathbf{n}_{P,j}) = \begin{bmatrix} \text{var}_{\delta \mathbf{n}_{P,j},x} & 0 & 0 \\ 0 & \text{var}_{\delta \mathbf{n}_{P,j},y} & 0 \\ 0 & 0 & \text{var}_{\delta \mathbf{n}_{P,j},z} \end{bmatrix}$$

$$\text{cov}(\delta \mathbf{p}_0) = \begin{bmatrix} \text{var}_{\delta \mathbf{p}_0,x} & 0 & 0 \\ 0 & \text{var}_{\delta \mathbf{p}_0,y} & 0 \\ 0 & 0 & \text{var}_{\delta \mathbf{p}_0,z} \end{bmatrix}$$

$$\text{cov}(\delta \mathbf{p}_{j,1}) = \begin{bmatrix} \text{var}_{\delta \mathbf{p}_{j,1},x} & 0 & 0 \\ 0 & \text{var}_{\delta \mathbf{p}_{j,1},y} & 0 \\ 0 & 0 & \text{var}_{\delta \mathbf{p}_{j,1},z} \end{bmatrix}$$

where $\text{var}_{\delta \mathbf{n}_{P,j}} = \text{var}_{\delta \mathbf{n}_{P,j},x} + \text{var}_{\delta \mathbf{n}_{P,j},y} + \text{var}_{\delta \mathbf{n}_{P,j},z}$,

$\text{var}_{\delta \mathbf{p}_0} = \text{var}_{\delta \mathbf{p}_0,x} + \text{var}_{\delta \mathbf{p}_0,y} + \text{var}_{\delta \mathbf{p}_0,z}$ and $\text{var}_{\delta \mathbf{p}_{j,1}} = \text{var}_{\delta \mathbf{p}_{j,1},x} + \text{var}_{\delta \mathbf{p}_{j,1_0},y} + \text{var}_{\delta \mathbf{p}_{j,1},z}$.

The variance of a single point $\mathbf{p}_{j,1}$ and the centroid $\mathbf{p}_0$ can be estimated by $\text{var}_{\delta \mathbf{p}_0} \approx \frac{1}{N_0} \sigma^2$ and $\text{var}_{\delta \mathbf{p}_{j,1}} \approx \sigma^2$ respectively. Hence,

$$\text{var}_{\delta \mathbf{n}_{P,j}} = \frac{1}{\left| \mathbf{p}_{j,1} - \mathbf{p}_0 \right|^2} \left(\sigma^2 + \frac{1}{N_0} \sigma^2 \right) \tag{87}$$

As shown in (40), $\mathbf{n}_P$ is calculated with a LMS solution utilizing all the N_1 points on ℓ_1. The measurement noise of each individual scan is also assumed to be independent. Therefore, the over-all error on $\mathbf{n}_P$ can be estimated and over-bounded using:

41

$$\text{var}_{\delta n_P} \approx \frac{1}{N_1} \sum_{j=1}^{N_1} \frac{1}{\left| \mathbf{p}_{j,1} - \mathbf{p}_0 \right|^2} \left(\frac{1}{N_1} \sigma^2 + \frac{1}{N_0} \sigma^2 \right)$$
$$\leq \frac{1}{\left[\min_{j=1..N_1} \left(\left| \mathbf{p}_{j,1} - \mathbf{p}_0 \right| \right) \right]^2} \left(\frac{1}{N_1} + \frac{1}{N_0} \right) \sigma^2 \tag{88}$$

where $\min_{j=1..N_1} \left(\left| \mathbf{p}_{j,1} - \mathbf{p}_0 \right| \right)$ is the distance from $\mathbf{p}_0$ to ℓ_1.

The second component of the estimation error on ρ as defined by (83) can now be over-bounded with

$$\text{VAR} \left\{ \frac{1}{N_0 + N_1} \left\{ \sum_{j=0}^{N_0-1} \mathbf{p}_{j,0} + \sum_{k=0}^{N_1-1} \mathbf{p}_{k,1} \right\} \delta[\hat{\mathbf{n}}_{P_j}] \right\}$$
$$\leq \frac{\left| \frac{1}{N_0 + N_1} \left\{ \sum_{j=0}^{N_0-1} \mathbf{p}_{j,0} + \sum_{k=0}^{N_1-1} \mathbf{p}_{k,1} \right\} \right|^2}{\left[\min_{j=1..N_1} \left(\left| \mathbf{p}_{j,1} - \mathbf{p}_0 \right| \right) \right]^2} \left(\frac{1}{N_1} + \frac{1}{N_0} \right) \sigma^2 \tag{89}$$

Define d as the average distance from the LADAR to both ℓ_0 and ℓ_1:

$$d = \left| \frac{1}{N_0 + N_1} \left\{ \sum_{j=0}^{N_0-1} \mathbf{p}_{j,0} + \sum_{k=0}^{N_1-1} \mathbf{p}_{k,1} \right\} \right|$$

Combining equations (85) and (89), the over-all error on the distance from LADAR to planar surface "i" can be estimated as follows:

$$\sigma^2_{\rho_i} \leq \left(\frac{1}{N_0 + N_1} \right) \sigma^2 + \frac{d^2}{\left[\min_{j=1..N_1} \left(\left| \mathbf{p}_{j,1} - \mathbf{p}_0 \right| \right) \right]^2} \left(\frac{1}{N_0} + \frac{1}{N_1} \right) \sigma^2 \tag{90}$$

Equation (90) describes the relationship between the LADAR scan parameters and the accuracy of estimated distance. The estimate tends to have smaller error if there are large numbers of points on both scan lines (greater N_0 and N_1); or if the two lines are well separated from each other (greater value of $\min_{j=1..N_1} \left(\left| \mathbf{p}_{j,1} - \mathbf{p}_0 \right| \right)$). However, the estimate will become less accurate if each laser point is less accurate (greater σ^2); or the LADAR is further away from the surface (greater d). Obviously these observations agree with the general understanding on LADAR measurements.

Under certain circumstances equation (90) can be further simplified. For example, in an indoor environment, often times ℓ_0 and ℓ_1 are nearly in parallel to each other, and the LADAR is facing the surface. The ratio of distance d over $\min_{j=1..N_1} \left(\left| \mathbf{p}_{j,1} - \mathbf{p}_0 \right| \right)$ is

approximately the co-tangent of the elevation angle between ℓ_0 and ℓ_1,

$$ctg(\varphi) \approx \frac{d}{\left[\min_{j=1..N_1}\left(\left|\mathbf{p}_{j,1} - \mathbf{p}_0\right|\right)\right]}.$$

With ℓ_1 scanned from a 15 degree elevation angle, and at least 30 points on both ℓ_0 and ℓ_1, $\varphi = 15^\circ$, $N_0 = N_1 = 30$,

$$\sigma^2_{\rho_1} \le \left(\frac{1}{N_0 + N_1}\right)\sigma^2 + \frac{d^2}{\left[\min_{j=1..N_1}\left(\left|\mathbf{p}_{j,1} - \mathbf{p}_0\right|\right)\right]^2}\left(\frac{1}{N_0} + \frac{1}{N_1}\right)\sigma^2 \approx \sigma^2.$$

Remember that the error analysis is performed to estimate the covariance matrix defined in (82). With the above simplification, the covariance matrix can be over-bounded by $\mathbf{COV}_\rho = \text{diag}(2\sigma^2)$. Computer simulation has been used to validate the covariance analysis. It also shows that a moving feature that has the minimum detectable bias can be reliably isolated with the threshold defined in (77).

One possible shortcoming of the above integrity monitoring approach would be the observability. The method requires redundant measurements to detect a moving feature, which means at least four planar surfaces have to be included in position solution. There may be less than four surfaces in some indoor applications, which will cause unavailability of the integrity. In addition, the MDB in equation (77) only applies to a moving surface that has a changing distance in relative to the LADAR. Although rarely observed in practice, it is possible for a moving object to rotate around the LADAR while maintaining a constant distance. Such a surface would have an erroneous estimation of normal vector and consequently cause deviation in position and attitude solutions. However, it may be difficult to detect a moving feature at constant distance with the parity of position LMS.

As discussed in Section 3.5, the 3D LADAR algorithm not only enables 3-D position solutions, but also provides attitude estimation. The second task of integrity monitoring is to detect a moving feature from attitude solution residuals.

As pointed out in (70), given an initial estimation, the attitude can be solved via

$$\Delta\Omega = \left(\mathbf{H}_\Omega^T \cdot \mathbf{H}_\Omega\right)^{-1} \cdot \mathbf{H}_\Omega^T \cdot \Delta\hat{\mathbf{n}} \tag{91}$$

with

$$\Delta\mathbf{n} = \begin{bmatrix} \left(\hat{\mathbf{C}}_i^j\right)_0 \cdot \mathbf{n}_{i,1} - \mathbf{n}_{j,1} \\ ... \\ \left(\hat{\mathbf{C}}_i^j\right)_0 \cdot \mathbf{n}_{i,M} - \mathbf{n}_{j,M} \end{bmatrix}, \mathbf{H}_\Omega = \begin{bmatrix} -\mathbf{n}_{j,1} \times \\ ... \\ -\mathbf{n}_{j,M} \times \end{bmatrix}$$

Performing a QR decomposition of $\mathbf{H}_\Omega$ yields:

43

$$[\mathbf{Q}_\Omega \quad \mathbf{R}_\Omega] = qr(\mathbf{H}_\Omega)$$
$$\mathbf{Q}_{\Omega L} = \mathbf{Q}_\Omega(4:M\times 3, 1:M\times 3) \tag{92}$$

Provided equation (92), the residual can be calculated as follows:

$$\mathbf{e}_\Omega = \mathbf{Q}_{\Omega L}^T \varepsilon_\Omega \tag{93}$$

Similar to the position solution, the LMS parity residuals (93) can also contain noise and bias.

Let $\mathbf{Q}_\Omega^e = \mathbf{Q}_{\Omega L}^T$, and

$$\mathbf{e}_\Omega = \mathbf{Q}_\Omega^e(\mathbf{v}_\Omega + \mathbf{b}_\Omega) \tag{94}$$

Assuming that the normal vector errors on M planes are independent from each other, the covariance matrix of $\Delta\mathbf{n}$ can be over-bounded by:

$$COV(\Delta\mathbf{n}) = \begin{bmatrix} cov\left(\left(\hat{\mathbf{C}}_i^j\right)_0 \cdot \mathbf{n}_{i,1} - \mathbf{n}_{j,1}\right) & & \\ & \cdots & \\ & & cov\left(\left(\hat{\mathbf{C}}_i^j\right)_0 \cdot \mathbf{n}_{i,M} - \mathbf{n}_{j,M}\right) \end{bmatrix} \tag{95}$$
$$\leq diag\left(2 \cdot var_{\delta\mathbf{n}_p}\right)$$

and

$$COV(\Delta\Omega) = \left(\left(\mathbf{H}_\Omega^T \cdot \mathbf{H}_\Omega\right)^{-1} \cdot \mathbf{H}_\Omega^T\right) COV(\Delta\mathbf{n}) \cdot \left(\left(\mathbf{H}_\Omega^T \cdot \mathbf{H}_\Omega\right)^{-1} \cdot \mathbf{H}_\Omega^T\right)^T,$$
$$COV_e = \mathbf{Q}_\Omega^e \cdot COV(\Delta\mathbf{n}) \cdot \mathbf{Q}_\Omega^e{}^T \tag{96}$$

Define $C_{k\Omega}$ as the detection threshold for the kth element of the residual vector $\mathbf{e}_\Omega$, and $MDB_{\Omega_k}^e$ as the MDB for the kth element of the residual vector:

$$C_{k\Omega} = \gamma_\Omega \cdot \sqrt{COV_{\Omega(k,k)}^e}$$
$$MDB_{\Omega_k}^e = \beta_\Omega \cdot \sqrt{COV_{\Omega(k,k)}^e} \tag{97}$$
$$k = 1,\ldots,M\times 3 - 3$$

where $COV_{\Omega(k,k)}^e$ is the kth row, k^{th} column element of the residual covariance. Detection and isolation of a rotating feature has also been verified via computer simulation.

As can be noticed from (91) and (92), $\mathbf{H}_\Omega$ is a $M\times 3$ by $M\times 3$ matrix. The residual vector is 1 by $M\times 3$-3, which provides a far greater observability than the 1 by M-3 vector e defined in (76). In practice, the initial estimation of attitude is formed with two non-

collinear normal vectors. An additional normal vector provides additional integrity information. However, integrity monitoring with the attitude residuals has an apparent blind-spot. It only detects change in plane normal vectors, and thus cannot isolate a surface moving toward or away from the LADAR that keeps the same direction. The detection threshold defined in (97) can be used to aid the primary integrity monitor implemented on position solution residuals.

4.   Data collection with the 4-rotor UAV in an urban environment.

To verify the algorithms developed in the first two years of this effort, data from an actual UAV with a scanning LADAR sensor will be collected onboard Ohio University's Four-Rotor Flying Sensor Platform. This platform was developed by Michael Stepaniak and Caleb White as part of Michael Stepaniak's Ph.D. research and its developed is described in detail in his dissertation [27]. Figure 30 shows the current sensor platform.
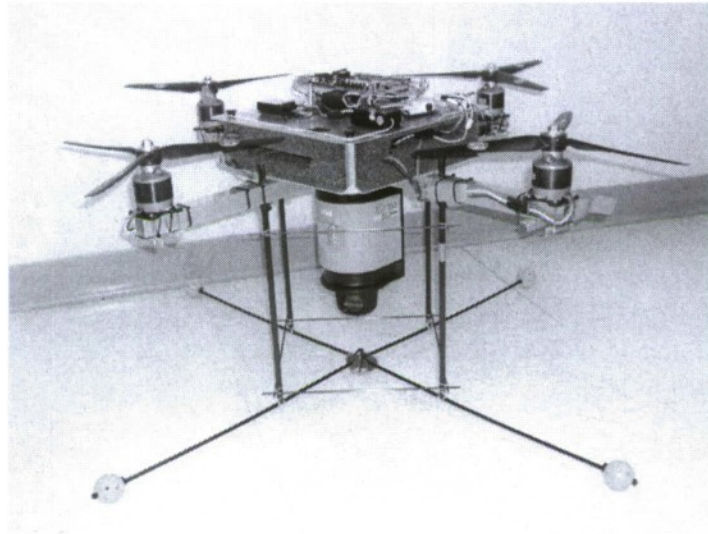

Figure 30. Four-rotor flying sensor platform

The basic concept behind the four-rotor sensor platform is that the UAV itself functions as the gimbals for the sensor onboard the UAV such as the 360-degree SICK scanning LADAR. By changing pitch and roll of the platform the multiple scans that are illustrated in Figures 8 and 9 can be performed.

Since the platform was only just completed, actual data collection efforts must still be performed. However, the interface of the processor with the SICK scanning LADAR and the HG1930 IMU has been completed. Two operational scenarios are currently envisions; one in which the scanning LADAR and IMU data are send to a data collection computer on the ground via a telemetry link based on 802.11b, and the other involves the installation of a low-weight data collection computer on the UAV itself.

5.   Conclusions

This report summarizes the investigation into the use of scanning 2D LADARs for autonomous navigation in three-dimensions. The navigation solution is based on planar surfaces extracted from LADAR scan images. The report describes a method for estimating plane parameters using images of a 2D scanning LADAR that is rotated in a limited elevation range (three different elevation angles are implemented). Changes in plane parameters between scans are applied to compute position and orientation changes. Least-squares linear position and attitude computation routines are presented. The use of DOP factors is introduced to formulate the influence of planar geometry on the navigation accuracy. Simulation results and test results presented demonstrate the feasibility of 3D navigation methods developed. Furthermore, a covariance analysis has been performed for the 3D autonomous navigation case. Finally, the 2D integrity equations developed in year 1 of the effort were extended to three dimensions.

A four-rotor flying sensor platform was developed and is currently being prepared for a data collection effort to verify and validate some of the proposed methodology using real UAV-based data. The planned sensors for this UAV are the SICK LD-OEM 360-degree scanning LADAR and the Honeywell HG1930 IMU. Interfaces for these sensors have been developed under efforts parallel to this one.

6.   Future work in Year 3

Originally year 3 would focus on the development of real-time urban UAV positioning and attitude determination algorithms that can be demonstrated on the 4-Rotor UAV (*task 3.1*). Although feature extraction and association algorithms have been developed during phases 1 and 2, real-time aspects would not be implemented until this Phase. Furthermore, real-time algorithms would be designed and implemented to perform an online mapping function (*task 3.2*). This phase would be concluded with a 4-Rotor UAV flight demonstration in an urban environment to demonstrate the feasibility of assured 3D position, attitude and heading determination (*task 3.3*). Even though the plan still includes the implementation of the algorithms onboard the UAV and a flight test with the UAV, the tasks in year 3 will also include the integration of scanning LADAR data with data from a 2D camera. Current work at Ohio University has shown potential for this integration mechanism and we think it is the logical extension for the research pursued in this effort since it addresses the observability drawbacks of LADAR-based navigation discussed in Section 4. Finally, the integrity methods developed in year 2 will be validated using Monte-Carlo simulations.

Reporting activities will consist of the semi-annual and final reports and an annual briefing.

7.   References

[1]   Soloviev, A., D. Bates, F. van Graas, "Tight Coupling of Laser Scanner and Inertial

Measurements for a Fully Autonomous Relative Navigation Solution," *NAVIGATION Journal of the Institute of Navigation*, Vol. 54, No. 3, 2007.

[2]   Altermatt, M., Martinelli, A., Tomatis, N., and R. Siegwart, *SLAM with Corner Features Based on a Relative Map*, In Proceedings of the International Conference on Intelligent Robots and Systems, Vol. 2, 2004.

[3]   Borges, G. A. and M.-J. Aldon, *Line Extraction in 2D Range Images for Mobile Robotics*, Journal of Intelligent and Robotic Systems, Vol. 40, Issue 3, 2004.

[4]   Pfister, S., Roumeliotis, S., and J. Burdick, *Weighted Line Fitting Algorithms for Mobile Robot Map Building and Efficient Data Representation*, In Proceedings of the IEEE International Conference on Robotics and Automation, 2003.

[5]   Pfister, S., Kriechbaum, K., Roumeliotis S., and J. Burdick, *Weighted Range Sensor Matching Algorithms for Mobile Robot Displacement Estimation*, In Proceedings of the IEEE International Conference on Robotics and Automation, ICRA, 2002.

[6]   Oskarsson, M. and K. Astrom, Accurate and Automatic Surveying of Beacon Positions for a Laser Guided Vehicle, In Progress in Industrial Mathematics at ECMI 98, 1999.

[7]   Bates, D. P., Navigation Using Optical Tracking of Objects at Unknown Locations, Master's Thesis, Ohio University, March 2007.

[8]   Diosi, A. and L. Kleeman, *Uncertainty of Line Segments Extracted from Static SICK PLS Laser Scans*, In Proceedings of the Australian Conference on Robotics and Automation, 2003.

[9]   Vadlamanai, A. K. and M. Uijt de Haag, *Use of Laser Range Scanners for Precise Navigation in Unknown Environments*, In Proceedings of the ION GNSS, 2006.

[10]   Hoshizaki, T., Andrisani II, D., Braun, A. W., Mulyana, A. K., and J. S. Bethel, *Performance of Integrated Electro-Optical Navigation Systems*, Navigation: Journal of the Institute of Navigation, Vol. 51, No. 2, 2004.

[11]   Joerger, M. and B. Pervan, *Range-Domain Integration of GPS and Laser-scanner Measurements for Outdoor Navigation*, In Proceedings of the ION GNSS, 2006.

[12]   Parkinson, B. W., and Axelrad P., "Autonomous GPS Integrity Monitoring Using The Pseudorange Residual," *NAVIGATION Journal of the Institute of Navigation*, Vol. 35, No. 2, 1988, pp. 255-274.

[13]   Sturza, M. A., "Navigation System Integrity Monitoring Using Redundant Measurements," *NAVIGATION Journal of the Institute of Navigation*, Vol. 35, No. 4, 1988, pp. 483-502.

[14]   Ren D., and Lin, C.-F. "Failure Detection and Isolation Structure for Global Positioning System Autonomous Integrity Monitoring," *Journal of Guidance, Control, and Dynamics*, Vol.18, No.2, 1995, pp 291-297.

[15]   Pervan, B., and Chan F.-C., "Detecting Global Positioning Satellite Orbit Errors Using Short-Baseline Carrier-Phase Measurements," *Journal of Guidance, Control, and Dynamics*, Vol. 26, No.1, 2003, pp. 122-131.

[16]   W. Kabsch, "A Discussion of the Solution for the Best Rotation to Relate Two Sets of Vectors," *Acta Crystallographica*, 34, 827-828.

[17]   Berthold K. P. Horn, "Closed-form solution of absolute orientation using unit quaternions," *Journal of the Optical Society of America*, 4:629-642.

[18]   A. Soloviev, D. Bates, and F. van Graas, "Tight Coupling of Laser Scanner and Inertial Measurements for a Fully Autonomous Relative Navigation Solution," *NAVIGATION, Journal of the Institute of Navigation*, Vol. 54, No. 3, Fall 2007, pp. 189-205.

[19]   S. Thrun, C. Martin, Y. Liu, D. Hahnel, R. Emery-Montemerlo, D. Chakrabarti, and W. Burgard, "A Real-Time Expectation Maximization Algorithm for Acquiring Multi-Planar Maps of Indoor Environments with Mobile Robots", *IEEE Transactions on Robotics and Automation*, 20(3) , June 2004, pp. 433-442.

[20]   Nguyen, V., Martinelli, A., Tomatis, N., and R. Siegwar, *A Comparison of Line Extraction Algorithms using 2D Laser Rangefinder for Indoor Mobile Robotics*, In Proceedings of the IEEE Conference on Intelligent Robots and Systems, IROS, 2005.

[21]   D. Bates and F. van Graas "Covariance Analysis Considering the Propagation of Laser Scanning Errors use in LADAR Navigation," in Proceedings of the Institute of Navigation Annual Meeting, Apr. 2007, pp. 624-634.

[22]   E. Kaplan and C. Hegarty (Editors), *Understanding GPS: Principles and Applications*, 2nd ed. Norwood Massachusetts, USA: Artech House, 2006.

[23]   G. Wahba, "A Least Squares Estimate of Satellite Attitude," *SIAM Review*, Vol. 7, No. 3, July 1965, p. 409.

[24]   M.L. Psiaki, "Attitude-Determination Filtering via Extended Quaternion Estimation," *Journal of Guidance, Control, and Dynamics*, Vol. 23, No. 2, March-April 2000, pp. 206-214.

[25]   K. Mostov, A. Soloviev, and T. J. Koo, "Initial Attitude Determination and

Correction of Gyro-Free INS Angular Orientation on the Basis of GPS Linear Navigation Parameters," in Proceedings of IEEE Conference on Intelligent Transportation Systems, Nov. 1997, pp. 1034-1039.

[26]   D. H. Titterton and J. L. Weston, *Strapdown Inertial Navigation Technology*, Second Edition, Reston, Virginia, USA and Stevenage, United Kingdom: The American Institute of Aeronautics and Astronautics, and The Institute of Electrical Engineers, 2004.

[27]   M. J. Stepaniak, "A Quadrotor Sensor Platform," Ph.D. Dissertation, Ohio University, August 2008.